



Repositorio Institucional de la Universidad Autónoma de Madrid

<https://repositorio.uam.es>

Esta es la **versión de autor** del artículo publicado en:

This is an **author produced version** of a paper published in:

Journal of Proteomics 113 (2015): 38-56

DOI: <http://dx.doi.org/10.1016/j.jprot.2014.09.007>

Copyright: © 2014 Elsevier

El acceso a la versión del editor puede requerir la suscripción del recurso

Access to the published version may require subscription

Differential proteomic profiling unveils new molecular mechanisms associated with mitochondrial complex III deficiency

Lorena Marín-Buera,^{1,2,§} Alberto García-Bartolomé,^{1,2,§} María Morán,^{1,2} Elia López-Bernardo,^{3,4} Susana Cadenas,^{3,4} Beatriz Hidalgo,⁵ Ricardo Sánchez,⁵ Sara Seneca,⁶ Joaquín Arenas,^{1,2} Miguel A. Martín,^{1,2} and Cristina Ugalde^{1,2,*}

[§]These authors contributed equally to this work

¹Instituto de Investigación, Hospital Universitario 12 de Octubre, Madrid 28041, Spain;

²Centro de Investigación Biomédica en Red de Enfermedades Raras (CIBERER), U723,

Madrid, Spain; ³Centro de Biología Molecular "Severo Ochoa" (CSIC-UAM) and

Departamento de Biología Molecular, Universidad Autónoma de Madrid, 28049

Madrid, Spain; ⁴Servicio de Inmunología, Hospital Universitario de La Princesa,

Instituto de Investigación Sanitaria Princesa (IP), 28006 Madrid, Spain; ⁵Servicio de

Bioquímica, Hospital Universitario 12 de Octubre, Madrid 28041, Spain, and ⁶Center of

Medical Genetics, AZ-VUB, Brussels, Belgium.

*Corresponding author: Dr. Cristina Ugalde, Centro de Investigación, Hospital

Universitario 12 de Octubre. Avda. de Córdoba s/n. 28041 Madrid. Phone: +34 91 779

2784, FAX: +34 91 390 8544, e-mail: cugalde@h12o.es

KEYWORDS: Mitochondria, OXPHOS system, respiratory chain, complex III deficiency, BCS1L, 2D-DIGE

ABSTRACT

We have analyzed the cellular pathways and metabolic adaptations that take place in primary skin fibroblasts from patients with mutations in *BCS1L*, a major genetic cause of mitochondrial complex III enzyme deficiency. Mutant fibroblasts exhibited low oxygen consumption rates and intracellular ATP levels, indicating that the main altered molecular event probably is a limited respiration-coupled ATP production through the OXPHOS system. Two-dimensional DIGE and MALDI-TOF/TOF mass spectrometry analyses unambiguously identified 39 proteins whose expression was significantly altered in complex III-deficient fibroblasts. Extensive statistical and cluster analyses revealed a protein profile characteristic for the *BCS1L* mutant fibroblasts that included alterations in energy metabolism, cell signaling and gene expression regulation, cytoskeleton formation and maintenance, and intracellular stress responses. The physiological validation of the predicted functional adaptations of human cultured fibroblasts to complex III deficiency confirmed the up-regulation of glycolytic enzyme activities and the accumulation of branched-chain among other amino acids, suggesting the activation of anaerobic glycolysis and cellular catabolic states, in particular protein catabolism, together with autophagy as adaptive responses to mitochondrial respiratory chain dysfunction and ATP deficiency. Our data point to an overall metabolic and genetic reprogramming that could contribute to explain the clinical manifestations of complex III deficiency in patients.

BIOLOGICAL SIGNIFICANCE

Despite considerable knowledge about their genetic origins, the pathophysiological mechanisms that contribute to the clinical manifestations of mitochondrial disorders remain poorly understood. We have investigated the molecular pathways and metabolic adaptations that take place in primary skin fibroblasts from patients with mutations in the *BCS1L* gene, a primary cause of mitochondrial complex III enzyme deficiency. Two-dimensional DIGE together with MALDI-TOF/TOF mass spectrometry and physiological validation analyses revealed a significant metabolic and genetic reprogramming as an adaptive response to mitochondrial respiratory chain dysfunction. Our data provide information about specific protein targets that regulate the trans-mitochondrial functional responses to complex III deficiency, thereby opening new doors for future research.

INTRODUCTION

Mitochondria participate as key regulators of cellular metabolism in a large variety of physiological processes, and provide most of the cellular energy (ATP) through the oxidative phosphorylation (OXPHOS) system. The OXPHOS system is located in the mitochondrial inner membrane and it is formed by five multiprotein enzyme complexes that couple respiration and ATP synthesis. Among these, respiratory chain cytochrome *bc*1 complex (or complex III) catalyzes the transfer of electrons from reduced coenzyme Q to cytochrome *c* associated with proton pumping to the intermembrane space [1]. The purified bovine complex is a ~450 kDa symmetric homodimer [2, 3]. Each monomer is composed of three catalytic subunits (cytochrome *b*, cytochrome *c*1 and the Rieske Iron-Sulfur Protein, or RISP) and eight structural subunits of unknown function.

Isolated complex III enzyme deficiencies cause a broad spectrum of symptoms that display tissue specificity in humans [4]. They are caused by mutations in catalytic and structural subunits as well as in assembly factors [5-10]. So far, the vast majority of mutations leading to complex III deficiency have been localized to the nuclear *BCS1L* gene, which encodes a mitochondrial inner membrane translocase necessary for the import and insertion of the RISP subunit into complex III [11]. *BCS1L* mutations lead to three main clinical phenotypes [12]: (1) Björnstad Syndrome, an autosomal recessive disorder characterized by sensorineural hearing loss and *pili torti* [13]; (2) GRACILE Syndrome, a Finnish-heritage disease caused by the homozygous p.Ser78Gly mutation [14], which is characterized by fetal growth retardation, aminoaciduria, cholestasis, iron overload, lactic acidosis, and early death; and (3) Complex III deficiency in neonates, infants or adults presenting with liver disease and lactic acidosis, alone or in combination with encephalopathy and visceral involvement [6, 15-21].

The pathophysiological mechanisms that contribute to the clinical manifestations of *BCS1L* mutations remain poorly understood. Mutations in *BCS1L* may lead to mitochondrial complex III assembly and enzyme defects in patients with Björnstad Syndrome or complex III deficiency [13, 17, 22], as well as in late stages of GRACILE Syndrome in *Bcs1l* transgenic mice [23]. This has been proposed to increase oxidative stress through the production of reactive oxygen species (ROS) in a mutation-dependent manner [13, 22]. A study from our group established a correlation between the severity of the clinical manifestations of complex III deficiency and specific cellular pathophysiological parameters in skin fibroblasts from six patients harboring mutations in the *BCS1L* gene [22]. Cells from patients with the most severe clinical phenotypes exhibited the slowest growth rates in glucose medium, displayed severe enzyme deficiencies and assembly defects of the respiratory chain complexes, increased ROS levels and unbalanced expression of the cellular antioxidant defenses, fragmented mitochondrial networks and increased cell death rates [22]. In agreement, *BCS1L* knockdown in human cells caused the disassembly of the mitochondrial supercomplexes and led to morphological alterations of the mitochondrial network [24]. On the contrary, Finnish patients with GRACILE syndrome exhibited normal complex III activity [14], and the fact that *BCS1L* functions as a mitochondrial translocase suggests that this protein could have broader functional implications than complex III assembly. Iron overload is also a common feature of patients with *BCS1L* mutations leading to GRACILE syndrome or complex III deficiency, which suggests an additional hypothetical role for *BCS1L* in iron metabolism [14, 16, 25].

To further identify the mechanisms underlying complex III deficiency, we have undertaken a combination of functional studies and high-resolution differential proteomics in cultured skin fibroblasts from four complex III-deficient patients harboring mutations in the *BCS1L* gene and four healthy controls. Mutant fibroblasts

1 showed significantly lower oxygen consumption rates and intracellular ATP levels than
2 controls. Subsequent two-dimensional differential gel electrophoresis (2D-DIGE) and
3 MALDI-TOF/TOF mass spectrometry analyses revealed a protein profile characteristic
4 for the *BCS1L* mutant fibroblasts that involved alterations in the energy metabolism,
5 cytoskeleton formation and maintenance, regulation of gene and protein expression, cell
6 signaling and the cellular stress responses. Physiological validation analyses suggested
7 the activation of anaerobic glycolysis, cellular catabolism and autophagy as main
8 adaptive responses to mitochondrial respiratory chain dysfunction and ATP deficiency.
9 These data represent novel starting points for elucidating the molecular mechanisms of
10 complex III deficiency.

MATERIAL AND METHODS

Fibroblast cultures

Primary skin fibroblasts from four patients and four healthy donors (age and sex-matched) were cultured in 1 g/l glucose-containing Dulbecco's modified Eagle's Medium (DMEM) (Invitrogen) supplemented with 10% fetal bovine serum (FBS), 100 IU/ml penicillin and 100 IU/ml streptomycin at 37°C and 5% CO₂. Mycoplasma testing was performed in fibroblasts by DAPI staining and epifluorescence microscopy, which yielded negative results. Control and patients' cells were balanced for passage number (9-10 passages).

Cell respiration

Oxygen consumption in human fibroblasts was measured using an XF24 Extracellular Flux Analyzer (Seahorse Bioscience). To obtain a homogeneous monolayer of cells, around 5.0×10^4 cells per well were plated the day before the experiment, depending on the growth rate of each cell line, and in order to obtain about 15 µg protein per well on the day of the experiment. The cells were then incubated for 1 h in unbuffered DMEM supplemented with 1 g/l glucose, 1 mM sodium pyruvate and 2 mM glutamine at 37°C in a CO₂-free incubator. In all experiments, the protein concentration in each well was determined using the Pierce BCA Protein Assay Kit (Thermo Scientific) after cell lysis in RIPA buffer (Sigma), and was used to calibrate the oxygen consumption data.

ATP content measurements

Intracellular ATP was measured in fibroblasts grown in DMEM-glucose culture medium using the ATP Bioluminescence Assay Kit HS II (Roche) according to manufacturer's instructions. ATP concentration was calculated per 10⁶ cells and expressed as percentage of control cells' ATP concentration.

Protein extraction for DIGE analysis

Whole protein extracts were prepared for each cell line. Samples were cleaned with the 2D Clean-up Kit (GE Healthcare) and stored overnight in acetone at -20 °C. Pellets were resuspended in 50 µl DIGE Buffer (10 mM Tris, 7 M urea, 2 M thiourea, 2% CHAPS). Protein concentration was determined using the Bradford reagent (BioRad).

DIGE Experimental Design and Protein Labeling

The proteomics comparison between whole protein extracts from four controls (C) and four patient-derived (P) fibroblasts was performed across four DIGE gels using the same pooled sample internal standard (consisting on an equal mix of the eight samples in the experiment) to reduce inter gel variations. This allows the straight comparison of all samples regardless how the sample pairings were selected. Proteins in each sample were fluorescently tagged with a set of matched fluorescent dyes according to the manufacturer's protocol for minimal labeling (GE Healthcare). To eliminate any dye-specific labeling artifacts, two samples of each group (C and P) were labeled with Cy3, and the other two were labeled with Cy5. The pooled sample internal standard was always Cy2-labeled. In every case, 400 pmol of dye was used for 50 µg of protein. Briefly, labeling was performed for 30 min on ice in darkness, and the reaction was quenched with 1 µl of 10 mM L-lysine for 10 min under the same conditions.

2D Electrophoresis and Imaging of Cy-labeled Proteins

The four pairs of Cy3- and Cy5-labeled samples (each containing 50 µg of protein) were combined and mixed with a 50 µg aliquot of the Cy2-labeled pooled standard. The mixtures containing 150 µg of protein were diluted 1:1 with rehydration buffer (7 M urea, 2 M thiourea, 4% CHAPS, 4% ampholytes (pH 3–11), and 200 mM DTT). The IPG strips (24 cm, nonlinear pH 3–11) were rehydrated overnight with 450 µl of a rehydration buffer as above but with 2% ampholytes, 0.002% bromophenol blue,

and 97 mM DeStreak reagent instead of DTT. The labeled samples were then applied to the strips by cup loading on a manifold equipped IPGphor II IEF system (GE Healthcare). Isoelectric focusing was carried out for a total of 75 kVh using the following conditions: 1 h at 120 V, 2 h at 500 V, gradient from 500 V to 1000 V in 2 h, gradient from 1000 V to 5000 V in 6 h, and finally 10 h at 5000 V. Prior to the second dimension run, the strips were equilibrated first for 12 min in equilibration buffer (100 mM Tris-HCl (pH 8.0), 6 M urea, 30% glycerol, 2% DTT and 2% SDS) and then for another 5 min in the same buffer supplemented with 2.5% iodoacetamide. The equilibrated strips were transferred onto 12% homogenous polyacrylamide gels (2.6% C) cast in low fluorescence glass plates using an Ettan-DALT six system (GE Healthcare). Electrophoresis was run at 1 W/gel for about 18 h at 20 °C.

The differentially labeled co-resolved proteins within each gel were imaged at a resolution of 100 dots/inch using a Typhoon 9400 laser scanner (GE Healthcare). Cy2-, Cy3-, and Cy5-labeled images of each gel were acquired at excitation/emission values of 488/520, 523/580, and 633/670 nm, respectively. Gels were scanned directly between the glass plates, and the high resolution images (pixel size 100 µm) were exported for data analysis. After imaging for Cy dyes, the gels were removed from the plates and subjected to colloidal Coomassie staining.

DIGE Data Analysis

The DeCyder v6.5 software (GE Healthcare) was used for spot detection and determination of quantity, inter gel matching, and statistics. The differential in gel analysis (DIA) module was used for automatic spot detection and abundance measurements for each individual gel by comparing the normalized volume ratio of each spot from a Cy3- or Cy5-labeled sample to the corresponding Cy2 signal from the pooled sample internal standard. The DIA data sets from each individual gel were collectively analyzed using the biological variation analysis (BVA) module, which

allows inter gel matching and calculation of average abundance for each protein spot among the four gels of our study. Statistical significance was assessed for each change in abundance using Student's *t* test and analysis of variance analyses. We considered statistical significance to be at the 95% confidence level ($p < 0.05$) when standardized average spot volume ratios exceeded 1.2 in the four analyzed gels (*i.e.* 12 analyzed images). Calculation of experimental molecular weight and pI for each differential protein spot was carried out using the PDQuest 7.3.1 computer software (Biorad).

Unsupervised principal component analysis (PCA), hierarchical clustering (HC), and *k*-means clustering analyses were performed using the DeCyder extended data analysis module on the group of spots identified as significantly changed. These multivariate analyses clustered the individual Cy3- and Cy5-labeled samples based on collective comparison of expression patterns from the set of proteins. The groups of protein expression characteristics are represented by each data point in the PCA plots and by each column in the HC expression matrixes.

Mass Spectrometry Analysis

The gel spots of interest were manually excised from the gels and transferred to microcentrifuge tubes. Samples selected for analysis were washed twice with water, shrunk with 100% ACN, and dried in a Savant SpeedVac. Then samples were reduced with DTT, alkylated with iodoacetamide, and subsequently digested with 12.5 ng/ μ l sequencing grade trypsin (Roche Applied Science) for at least 6 h at 37 °C. After digestion, the supernatant was collected, and 1 μ l was spotted onto a MALDI target plate (384 spot Teflon®-coated plates) and allowed to air dry at room temperature. Subsequently, 0.5 μ l of a 3 mg/ml solution of α -cyano-4-hydroxy-*trans*cinnamic acid matrix in 0.1% TFA and 50% ACN was added to the dried peptide digest spots and again allowed to air dry. The samples were analyzed using the MALDI-TOF/TOF mass

spectrometer 4800 Proteomics Analyzer and 4000 Series Explorer™ software (Applied Biosystems). MALDI-TOF spectra were acquired in reflector positive ion mode using 1000 laser shots per spectrum. Data Explorer version 4.2 (Applied Biosystems) was used for spectra analyses and generating peak picking lists. All mass spectra were internally calibrated using autoproteolytic trypsin fragments and externally calibrated using a standard peptide mixture (Sigma Aldrich). TOF/TOF fragmentation spectra were acquired by selecting the 10 most abundant ions of each MALDI-TOF peptide mass map (excluding trypsin autolytic peptides and other known background ions) and averaging 2000 laser shots per fragmentation spectrum. The parameters used to analyze the data were a signal to noise threshold of 20, a minimum area of 100, and a resolution higher than 10,000 with a mass accuracy of 20 ppm.

Online Tools and Database Search

The monoisotopic peptide mass fingerprinting data obtained from MS and the amino acid sequence tag obtained from each peptide fragmentation in MS/MS analyses were used to search for protein candidates using Mascot version 1.9 (Matrix Science). Peak intensity was used to select up to 50 peaks per spot for peptide mass fingerprinting and 50 peaks per precursor for MS/MS identification. Tryptic autolytic fragment-, keratin-, and matrix-derived peaks were removed from the data set used for the database search. The searches for peptide mass fingerprints and tandem MS spectra were performed in the Swiss-Prot release 53.0 and TrEMBL release 37.0 databases without taxonomy restriction, containing 269,293 and 4,672,908 sequence entries, respectively, for each software version and database release. Fixed and variable modifications were considered (Cys as *S*-carbamidomethyl derivative and Met as oxidized methionine, respectively), allowing one trypsin missed cleavage site and a mass tolerance of 50 ppm. For MS/MS identifications, a precursor tolerance of 50 ppm and MS/MS fragment tolerance of 0.3 Da were used. Identifications were accepted as positive when at least

five matching peptides and at least 20% of the peptide coverage of the theoretical sequences matched within a mass accuracy of 50 or 25 ppm with internal calibration. In every case probability scores were significant at $p < 0.01$.

Intracellular localization of the identified proteins was predicted from the amino acid sequence using the PSORT II software (<http://psort.hgc.jp/form2.html>). Mapping of proteins identified by mass spectrometry, and database search onto existing pathways and cellular networks was carried out using the KEGG Pathway (<http://www.genome.jp/kegg/pathway.html>) and STRING 9.1 (<http://string-db.org/>) Databases [26, 27].

Western-blot analysis

The supernatants (corresponding to 10 µg of whole cell extracts) were mixed with an equal volume of tricine sample buffer (Biorad) containing 2% (v/v) 2-mercaptoethanol. The mixtures were boiled for 5 min and proteins were separated on standard 10% SDS-PAGE gels and transferred onto PROTRANTM nitrocellulose membranes (Whatman[®]). Membranes were blocked in phosphate-buffered saline (pH 7.4) containing 0.1% Tween-20 and 5% non-fat dried milk for at least 2 hours at room temperature. The blots were then hybridized with antibodies raised against the following proteins: lamin-A/C (Santa Cruz), gelsolin (Abcam), glyceraldehyde 3 phosphate dehydrogenase (Mitosciences), DJ-1 (Abcam) and β-actin (Sigma). Peroxidase-conjugated anti-mouse or anti-rabbit IgGs (Molecular Probes) were used as secondary antibodies. Immunoreactive bands were detected by chemiluminescence with ECL[®] prime reagents (Amersham Biosciences) in a G:Box Chemi IR6 Image Analyzer (Syngene). Quantitative changes in band intensities were evaluated by densitometric scanning with the Image J software and the densitometric values were normalized to those of the loading controls.

Indirect Immunofluorescence

Cells were fixed with 4% paraformaldehyde for 15 min and permeabilized for 15 min with 0.1% Triton X-100. Cells were incubated in blocking buffer containing 10% goat serum for 1h at room temperature. Immunodetection was performed with the previously mentioned primary antibodies, and FITC (MitoSciences) and Alexa 488 (Invitrogen) were used as secondary antibodies. After appropriate rinsing, cover slips were mounted in ProLong Gold antifade reagent (Molecular Probes) on glass slides, and cells were viewed with a Zeiss LSM 510 Meta confocal microscope and a 63x planapochromat objective.

Amino acids concentrations of cell culture media

Approximately 1.5×10^6 fibroblasts were plated and cultured for 48 hours in serum-free DMEM supplemented with 100 IU/ml penicillin/streptomycin at 37°C and 5% CO₂. Cell culture media were collected and the samples (200 µL) were deproteinized for 20 minutes with 20 µL of 50% sulfosalicylic acid, centrifuged, and the protein-free supernatant was mixed with a lithium citrate buffer (1:1). Cationic exchange chromatography was performed with a stepwise elution of free amino acids with citrate buffers and detection with ninhydrin, using a Biochrom 30 amino acid analyzer (Biochrom Ltd.) according to the manufacturer's specifications. The amino acids concentrations were expressed in µmol/L. The protein concentration on each sample was determined with the Pierce BCA Protein Assay Kit (Thermo Scientific) and used to normalize the amino acid concentration data.

GAPDH and PDH enzyme activities

Glyceraldehyde-3-phosphate dehydrogenase (GAPDH) activity was measured using a colorimetric GAPDH Assay Kit (ScienCell™) and pyruvate dehydrogenase (PDH) activity was determined using the PDH Enzyme Activity Dipstick Assay Kit

(Mitosciences), according to the manufacturers' protocols. Enzyme activities were normalized by the protein concentration on each sample.

Data Analysis

Unless indicated, all experiments were performed at least in triplicate and results were presented as mean \pm standard deviation (SD) values. Statistical p values were obtained by application of either Student's t test or Mann-Whitney U test using the SPSS v15.0 program.

RESULTS

Decreased oxygen consumption and ATP levels in fibroblasts with mutations in *BCS1L*

To shed light on the metabolic alterations and signaling pathways affected by mitochondrial respiratory chain complex III enzyme deficiency, we first measured oxygen consumption rates (OCR), intracellular ATP levels and extracellular acidification rates (ECAR) in genetically and biochemically characterized primary skin fibroblasts from four healthy donors (C) and four complex III-deficient patients (P) harboring mutations in the *BCS1L* gene [15, 16, 18, 22]. Measurements showed a significant reduction of ~30% in the oxygen consumption rates (Figure 1A) and a decrease of ~70% in the intracellular ATP concentration (Figure 1B) of *BCS1L* mutant fibroblasts compared with the controls. No significant differences were observed in the extracellular acidification rates between these two sample groups (Figure 1C). The individual values obtained for each patient's cell line are shown in Supplemental Figure 1.

2D-DIGE analysis of fibroblasts with mutations in *BCS1L*

We next performed a 2D-DIGE proteomics analysis in whole cell extracts from eight samples corresponding to four controls and four fibroblasts with mutations in *BCS1L* (Figure 2). After four-plex 2D-DIGE, three individual images were obtained from each gel, corresponding to Cy2-, Cy3-, and Cy5-labeled samples. The 12 gel images were analyzed using the DeCyder software. DIA allowed the detection of an average of 1817 protein spots on each image with a 2.73 % coefficient of variation between them. Then inter image spot matching was carried out by BVA. In this step, an average of 1456 spots was matched on the gels (2.71 % coefficient of variation), and their average abundances among the 12 images of our study were calculated. We considered changes within a 95% confidence interval ($p < 0.05$) and standardized

average spot volume ratios exceeding 1.2 in the four analyzed gels. This analysis yielded a total of 52 protein species common to the 12 gel images that were unambiguously identified as significantly altered in complex III deficiency: 34 spots were significantly and reproducibly increased in all four patients' fibroblasts relative to the four controls, and 18 spots were decreased. These 52 spots are depicted on a representative DIGE gel image shown in Figure 3.

Identification of differentially expressed proteins in complex III-deficient fibroblasts

For the identification of proteins, spots were selected, digested in gel, and analyzed by MALDI-PMF-MS. A Mascot database search using the PMF spectra allowed the identification of the proteins present in 39 out of the 52 spots obtained from duplicate gels (spots 7, 12, 29, 33, 35, 38, 40, 46, 47, 48, 49, 50 and 51 failed to be identified). In nine cases (spots 2, 9, 15, 21, 23, 24, 32, 39 and 52), two different proteins were identified on the same spot, and we also detected 16 redundancies because of posttranslational modifications or proteolysis. The last 7 proteins from the group of 52 were identified by tandem MS. Altogether 39 different proteins were identified as altered in *BCS1L*-associated complex III deficiency, as listed in Table 1 and Supplemental Table 1 with detailed information comprising experimental and theoretical molecular weight and pI values, accession number, and identification parameters.

Multivariate Statistical Analysis

We sought to establish biological significance of the protein changes by performing multivariate statistical tests on the proteins identified by DIGE-MS. As shown in Figure 4A, principal component analysis displayed a good separation of the control and patients' sample groups. For the 52 protein spots altered in the DIGE analysis, the first principal component (PC1) distinguished 73.9% of the variance, and

an additional 10.6% variation was distinguished by the second principal component (PC2). A second type of pattern analysis, the *k*-means algorithm, was carried out on these 52 protein forms. This analysis clustered them into four groups displaying similar patterns (Figure 4B). The proteins in each *k*-means cluster are listed in Supplemental Table S2. Finally, hierarchical clustering analysis (Figure 4C) established two different patterns in this group of proteins and clearly differentiated these two diverse profiles, clustering patients-derived (marked within a green square in Figure 4C) and control fibroblasts (orange square). Protein spot numbering indicated in the heat map correlates with the information shown in Table 1.

The variations in the expression levels of some of the proteins altered in the complex III deficient-fibroblasts were validated using Western-blot and immunofluorescence analyses (Figure 5). These analyses confirmed decreased levels of nuclear lamin-A/C, and increased levels of cytoplasmic gelsolin, glyceraldehyde 3 phosphate dehydrogenase (GAPDH), and the endoplasmic reticulum DJ-1 protein in the *BCS1L* mutant fibroblasts compared with the controls.

Cellular pathways altered in complex III-deficient fibroblasts

A database search was carried out to analyze the predicted subcellular localization of these proteins and to assign them into different functional groups. Most of the identified proteins were predicted as mainly cytosolic (69%), with an additional 15% being predicted as nuclear, 8% associated with other membrane structures or located in other subcellular organelles, such as the endoplasmic reticulum, vacuoles, or peroxisomes, and only 8% being predicted as purely mitochondrial.

Bioinformatics analysis using the KEGG Pathway and STRING 9.05 Databases [26, 27] enabled the characterization of biological association networks related to these differentially expressed proteins that allowed us to identify the biochemical pathways that could be altered in complex III deficiency. According to their specific cellular roles,

the 39 proteins whose expression was altered in the *BCS1L* mutant fibroblasts were divided into five different functional categories. The main protein group (31%) is involved in metabolic pathways that primarily regulate energy metabolism (specifically affecting glycolysis, the TCA cycle and the pentose phosphate and hexosamine pathways) and iron homeostasis. The remainder proteins are involved either in the regulation of gene expression at the levels of transcription, DNA replication or protein synthesis (23%), are structural or cytoskeleton- related (23%), take part in intracellular transport events and cell signaling (13%), or are either chaperones or regulatory proteins involved in cellular responses to metabolic and oxidative stress (10%).

We next aimed to physiologically validate some of the predicted functional adaptations of human cultured fibroblasts to mitochondrial complex III deficiency. Our DIGE analysis showed increased levels of two enzymes involved in the glycolytic pathway, glyceraldehyde 3-phosphate dehydrogenase (GAPDH) and α -enolase, suggesting the up-regulation of glycolysis as a way to produce ATP when the respiratory chain is malfunctioning. Triplicate spectrophotometric measurements revealed an increase of ~52% in the mean GAPDH enzyme activity of fibroblasts with mutations in *BCS1L* compared with that of the controls, suggestive of an up-regulation of the glycolytic flux (Figure 6A). Proteomics also revealed decreased levels of dihydrolipoyl dehydrogenase (DLD) in the *BCS1L* mutant fibroblasts. DLD is an enzyme involved in the mitochondrial glycine cleavage system, which is also a key component of the pyruvate dehydrogenase, alpha-ketoglutarate dehydrogenase, and branched-chain alpha-ketoacid dehydrogenase complexes, therefore playing crucial roles in key steps of the intermediary metabolism. Defects in DLD are involved in the development of maple syrup urine disease (MSUD) [OMIM: 248600], a metabolic disorder caused by an enzyme defect in the catabolic pathway of the branched-chain amino acids, which accumulate together with their corresponding keto acids, leading to

encephalopathy and progressive neurodegeneration [28]. As expected, the decreased DLD protein levels provoked a decrease of 43% in the mean PDH enzyme activity of patients' fibroblasts compared with the controls (Figure 6B). We next analyzed whether the reduced DLD levels in *BCSIL* mutant fibroblasts also led to the accumulation of its reaction precursors, such as glycine or branched-chain amino acids. Cells were grown for 48 hours in serum-free medium, and the amino acids concentrations from cell culture media were measured in triplicate (Figure 6C). A prominent increase in the concentration of the branched-chain amino acids leucine, isoleucine, and valine was observed in patients' fibroblasts compared with the controls, together with raised levels of other amino acids, such as glutamine, threonine, glycine, serine, cysteine, methionine, tyrosine, phenylalanine, lysine, histidine, tryptophan and arginine. These data support the alteration of branched-chain amino acids catabolism probably as a consequence of the DLD defect, although the increased levels of most amino acids could be indicative of a general activation of protein catabolism in complex III-deficient fibroblasts. Based in the results obtained from the DIGE and validation analyses, a hypothetical model of the physiological adaptations that take place in fibroblasts with mutations in *BCSIL* is proposed in Figure 7.

DISCUSSION

In this work we have analyzed the cellular and metabolic adaptations that take place in primary skin fibroblasts from patients with mitochondrial complex III deficiency. To identify these mechanisms, we undertook a high-resolution differential proteomic analysis of cultured skin fibroblasts from four complex III-deficient patients harboring diverse mutations in the *BCS1L* gene and four healthy controls. This experimental strategy yielded a total of 39 proteins successfully identified by mass spectrometry that were differentially expressed between control and patients' samples. The protein profile characteristic for *BCS1L*-associated complex III deficiency suggested alterations in pathways controlling energy metabolism and cellular homeostasis, cytoskeleton formation and maintenance, gene expression and protein synthesis, intracellular transport and signal transduction, and cell stress responses.

Metabolic alterations

The main proteins group whose expression was altered in the *BCS1L* mutant fibroblasts was involved in energy metabolism. In complex III-deficient fibroblasts the main altered molecular event is probably a limited respiration-coupled ATP production through the OXPHOS system, which would force a metabolic switch that would enable to obtain energy primarily from glycolysis and alternative catabolic processes, with a parallel reduction or blockage of alternative glucose- and ATP-consuming pathways, such as the phosphate pentose and hexosamine pathways, and a decreased TCA cycle.

During glycolysis, glucose is converted into pyruvate and the free energy released is used to form the energy-rich molecules ATP and NADH. In fibroblasts with *BCS1L* mutations this pathway is affected at the levels of three enzymes, presenting reduced levels of fructose-bisphosphate aldolase A (ALDOA), and increased levels of glyceraldehyde 3-phosphate dehydrogenase (GAPDH) and α -enolase. ALDOA catalyses the reversible conversion of fructose 1,6-bisphosphate into glyceraldehyde 3-

phosphate (G3P) and dihydroxyacetone phosphate (DHAP). Since ATP is required for the synthesis of fructose 1,6-bisphosphate in the first steps of glycolysis, it is possible that the reduced ALDOA levels are a consequence of the limited availability of its substrate. This would imply reduced levels of G3P and DHAP, which are necessary substrates for the glycolytic energy generation phase in which ATP and NADH are produced. The first step of this second phase of glycolysis is catalyzed by GAPDH, which converts G3P into D-glycerate 1,3-bisphosphate. α -enolase is responsible for the penultimate step of glycolysis in which the catalysis of 2-phosphoglycerate to phosphoenol pyruvate takes place. Therefore, the increased levels of GAPDH and α -enolase could take place as compensatory responses to increase the glycolytic flux efficiency and pyruvate biosynthesis, which in aerobic conditions is transformed through the pyruvate dehydrogenase complex into acetyl-CoA, usable in the mitochondrial TCA cycle to carry out cellular respiration and ATP production. However, in fibroblasts with mutations in *BCSIL* anaerobic glycolysis would not increase enough to compensate for a deficient oxidative phosphorylation, since ATP levels remained significantly lower in the patients' fibroblasts compared with controls.

Our proteomic analysis suggested alterations in both pyruvate conversion and the TCA cycle activities due to reduced levels of two key mitochondrial enzymes: dihydrolipoyl dehydrogenase (DLD) and dihydrolipoyl lysine-residue succinyltransferase (DLST). DLD is a multifunctional enzyme that catalyzes NADH oxidation and plays an important role in redox metabolism [29, 30]. DLD is a functional component of the pyruvate dehydrogenase complex, thus decreasing its levels could compromise the conversion of pyruvate into acetyl-CoA and lead to the accumulation of cytosolic pyruvate, which is probably transformed by the enzyme lactate dehydrogenase into lactate and NAD^+ to keep glycolysis active. The fact that *BCSIL* mutant fibroblasts did not generally present increased acidification of cell culture media suggests that,

despite glycolysis up-regulation, the accumulating pyruvate could undergo a rapid transamination to alanine in order to avoid environmental acidification. Besides, DLD is a component of the branched-chain α -ketoacid dehydrogenase complex (BCKDC), involved in the catabolism of branched-chain amino acids and their derivatives. Reduced DLD levels could therefore explain the accumulation of branched-chain amino acids observed in fibroblasts with mutations in *BCSIL*, although the general increase in amino acids levels might be indicative of a broader activation of protein catabolism. Both DLD and DLST are also components of the oxoglutarate dehydrogenase complex, which catalyzes the conversion of α -ketoglutarate to succinyl-CoA in the TCA cycle. Therefore, the decreased DLD and DLST levels could presumably compromise the normal flux and favor the accumulation of intermediate metabolites of the TCA cycle. In agreement with our results, the liver metabolomic profile of late disease stages of GRACILE Syndrome in transgenic mice showed decreased levels of G3P and DHAP, decreased activities and accumulation of intermediate metabolites of the TCA cycle, and increased levels of amino acids and long-chain acylcarnitines [31].

According to our data, the phosphate pentose (PP) pathway would also be down-regulated in favor of glycolysis, since both routes require glucose oxidation in their initial steps. There are two distinct phases in the PP pathway, the oxidative phase, in which most of the cellular reducing energy in form of NADPH is generated, and the non-oxidative phase, in which 5-carbon sugars are synthesized for nucleotide and nucleic acids biogenesis. The *BCSIL* mutant fibroblasts showed decreased levels of two initial PP pathway rate-limiting enzymes: glucose-6-phosphate dehydrogenase (G6PDH) and hexose-6-phosphate dehydrogenase (H6PD). G6PDH converts glucose-6-phosphate into 6-phosphoglucono- δ -lactone whilst reducing NADP^+ to NADPH. NADPH is necessary for lipid and nucleic acids biosynthesis, and it is used by the glutathione reductase enzyme to reduce glutathione, which is in turn oxidized by

1 glutathione peroxidase to convert reactive hydrogen peroxide (H_2O_2) into H_2O .
2 Therefore, NADPH re-oxidation constitutes an essential step to prevent the
3 accumulation of hydroxyl free radicals and to ensure protection against oxidative
4 damage. It is reasonable to expect that decreased G6PDH levels may hinder H_2O_2
5 detoxification by cutting the NADPH supply, which would explain the high H_2O_2 levels
6 and the alterations in the cellular antioxidant defenses previously observed in fibroblasts
7 with mutations in *BCSIL* [22]. H6PD is the initial component of the PP pathway inside
8 the endoplasmic reticulum (ER) that generates NADPH for ER enzymes, and its
9 blockage may activate the cellular stress response known as unfolded protein response
10 (UPR) [32], in agreement with the up regulation of the UPR proteins GRP78, ERP29
11 and ERP70 observed in the mutant fibroblasts (see ahead). The presumed reduction in
12 the levels of the G6PDH and H6PD reaction products could potentially provoke a
13 compensatory raise in the levels of the second enzyme of the PP pathway, 6-
14 phosphogluconolactonase (PGLS), as revealed by our DIGE analysis.

15 As a consequence to the partial blockage of the PP pathway, lipids as well as
16 nucleic acids biosynthesis would be hampered. Accordingly, reduced levels of C-1-
17 tetrahydrofolate synthase were detected. This enzyme participates in the synthesis of
18 tetrahydrofolate derivatives, essential cofactors used in amino acids metabolism and for
19 the synthesis of purines and pyrimidines. The *BCSIL* mutant fibroblasts also showed
20 increased levels of adenine phosphoribosyltransferase (APRT) and glucosamine-6-
21 phosphate isomerase 1 (GNPDA1). APRT catalyzes the formation of AMP from the
22 adenine rescued from DNA and RNA degradation in the purine nucleotide
23 salvage pathway, an essential route in cells unable to perform *de novo* synthesis of
24 nucleic and ribonucleic acids. These increased APRT levels agree with the AMP
25 accumulation detected in late disease stages of GRACILE Syndrome in transgenic mice
26 [31]. GNPDA1 participates in the hexosamine biosynthetic pathway, whose end-

products will be used for making glycosaminoglycans, proteoglycans, and glycolipids that are key structural components of cell membranes, extracellular matrix and connecting tissues. GNPDA1 catabolyzes the reversible conversion of D-glucosamine-6-phosphate into D-fructose-6-phosphate, which could be used as a direct substrate in the glycolitic pathway possibly at the expense of cellular structural components.

Noteworthy, the ferritin light chain (FTL) levels were increased in the *BCS1L* mutant fibroblasts. Ferritin is the primary intracellular iron-storage protein complex and keeps iron in a soluble and nontoxic state. It is composed of heavy and light ferritin chains, and variations in its subunits composition may affect the rates of iron uptake and release in human cells. Many patients harboring mutations in the *BCS1L* gene present with iron overload, increased ferritin levels and low iron binding capacities, and based on these clinical evidences, a role for *BCS1L* in iron homeostasis was proposed [14]. Since ferritin is up-regulated in response to different types of cellular stress [33], it is plausible to speculate that the increased FTL levels could constitute a secondary response to the metabolic and oxidative stresses generated by the *BCS1L* mutations.

Alterations in the regulation of gene and protein expression

The second proteins group involved those participating in the regulation of gene and protein expression, in agreement with the observed alterations in nucleic and amino acids metabolisms via blockage of the TCA cycle and the PP pathway. The *BCS1L* mutant cells showed reduced levels of the SND1, Lamin-A/C, XRCC6 and DDX1 proteins. SND1 is a component of the RNA-induced silencing complex (RISC) that plays a dual role in the regulation of transcription and pre-mRNA splicing [34]. Lamin-A/C is a constituent of the nuclear lamina, a protein matrix involved in nuclear stability, chromatin structure and gene expression that regulates cell cycle and apoptosis [35]. XRCC6 is a subunit of the ATP-dependent DNA helicase 2, which is required for the non-homologous end joining (NHEJ) pathway of DNA repair [36]. Alterations in

1 this pathway may cause genomic instability and cell cycle arrest and it is associated
2 with several human genetic syndromes [37]. The ATP-dependent RNA helicase DDX1
3 belongs to the DEAD box protein family, implicated in a number of cellular processes
4 that involve the modification of RNA secondary structures. This protein plays an RNA
5 clearance role at DNA double-strand break sites, thereby facilitating the template-
6 guided repair of transcriptionally active regions of the genome [38]. The *BCSIL* mutant
7 fibroblasts also exhibited mildly decreased levels of the eukaryotic translation initiation
8 factor EIF3H. These cells possibly compensate for those alterations by up-regulating
9 other gene expression regulatory proteins, such as cytoplasmic asparagine-tRNA ligase
10 (NARS), the abhydrolase domain-containing protein 14B (ABDH14B), or the
11 heterogeneous nuclear ribonucleoprotein Q (hnRNP Q). NARS contributes to the initial
12 steps of protein biosynthesis by activating and transferring asparagine to specific tRNA
13 molecules. ABDH14B is an unknown function enzyme that could be involved in
14 activating nuclear transcription [39]. HNRNPQ is an mRNA-binding protein implicated
15 in translation regulation through miRNA-mediated repression of specific mRNAs [40],
16 as well as in cellular stress responses by regulating p53 translation efficiency and
17 thereby, cell cycle and apoptosis progression [41]. In oxidative stress conditions p53 is
18 imported into mitochondria, where it interacts with the mitochondrial DNA (mtDNA)
19 single-stranded binding protein (mtSSB) to promote mtDNA repair [42]. In agreement,
20 the levels of the mtSSB protein, involved in mtDNA replication [43], were also raised.
21 Since increased mitochondrial proliferation is commonly associated with respiratory
22 chain defects, the mtSSB protein up-regulation would enable a dual oxidative stress-
23 induced response, allowing for the protection of mtDNA against oxidative damage
24 lesions in parallel with enhancing mitochondrial biogenesis to compensate for the
25 dysfunctional respiratory chain. These putative alterations in the regulation of gene and
26 protein expression are suggestive of cell survival adaptations that could ultimately affect

cell division and apoptosis. In this regard, the *BCS1L* mutant fibroblasts exhibited slow growth rates in glucose media and apoptotic cell death [22].

Alterations in cytoskeleton formation and maintenance

In eukaryotic cells, the cytoskeleton is composed of actin filaments, intermediate filaments and microtubules that play important roles in the organization and distribution of the internal cellular structures, in the intracellular transport of organelles and secretory vesicles, and in cellular division. The *BCS1L* mutant fibroblasts showed putative alterations in cytoskeleton formation through the reduced levels of a number of structural constituents, such as vinculin, moesin, or the WDR1 protein, which may function either as cross-linkers between plasma membranes and actin-based cytoskeletons or are involved in the assembly/disassembly of actin filaments, or such as vimentin, an intermediate filament scaffolding protein that plays a role in anchoring the organelles position in the cytosol, or alpha-tubulin, a major structural component of the microtubules. Cytoskeleton disorganization could thus take place as a consequence of the decreased levels of its key structural components, which could be potentially compensated by the up-regulation of regulatory proteins involved in the organization and assembly of these structures. Such could be the case for the Rho GTPase activating protein p50rhoGAP (or CDC42GAP), involved in actin cytoskeleton remodeling through the activation of signal transduction pathways from plasma-membrane receptors [44]; the dihydropyrimidinase-related protein CRMP-2, that regulates actin cytoskeleton organization and microtubules assembly [45]; septin-11, a cytoskeletal GTPase that associates with cellular membranes, actin filaments and microtubules, thus playing a role in cytoskeleton reorganization and cellular architecture maintenance [46]; or gelsolin, a calcium-dependent actin-binding protein that regulates actin filaments assembly and disassembly [47]. Since mitochondria are well known to bind and move along microtubules and actin filaments, a hypothetical deconstruction of

the cytoskeleton could explain the predominantly fragmented phenotype of the mitochondrial network in *BCS1L* mutant fibroblasts, in the absence of significant alterations in proteins involved in the mitochondrial fusion and fission processes [22].

Of note, cytoskeleton constituents may act as powerful regulatory checkpoints that directly impact mitochondrial metabolism. For instance, dimeric tubulin physically interacts with VDAC, a component of the major ion channel of the mitochondrial outer membrane, to regulate respiration and energy metabolism [48]. Most glycolytic enzymes have been shown to bind to microtubules, and their enzyme activities depend on the bound-unbound state [49]. By this type of control, cytoskeleton components could selectively adapt metabolic fluxes between mitochondria and the cytosol to alterations in metabolic conditions, and provide a functional link between mitochondrial metabolism, the internal cellular organization and cell cycle.

Alterations in intracellular trafficking and signal transduction

Complex III-deficient fibroblasts exhibited increased levels of proteins involved in cell signaling processes that couple gene expression to intracellular trafficking, such as the phosphatidylethanolamine-binding protein PEPBP1/RKIP, annexin 2, annexin 4 and sorting nexin 6 (SNX6). RKIP is a master modulator of the MAP kinases, NF- κ B and G-protein-mediated signaling pathways to control cellular growth, motility, apoptosis and genomic integrity [50]. Annexins are cytosolic proteins that bind negatively charged phospholipids present in the membrane walls in a Ca^{2+} -dependent manner [51]. Annexin 2 (ANXA2) is a multifunctional protein that binds PIP2 (phosphatidylinositol-4,5-bisphosphate) to facilitate actin assembly in the vicinity of the cell membrane [52], regulates post-transcriptional gene expression [53], and the biogenesis of multivesicular transport intermediates destined for late endosomes in the degradation pathway that leads to lysosomes [54]. Annexin A4 (ANXA4) is involved in the regulation of endo- and exocytosis, in ion-transport regulation and in the Ca^{2+} -

dependent modulation of the NF- κ B signaling pathway [55]. SNX6 is a component of the retromer complex that mediates the retrograde trafficking of membrane proteins from endosomes to the *trans*-Golgi network (TGN), essential for the retrieval of membrane receptors [56]. This protein links the retromer to the microtubule motor complex that allows the long-range movement of endosomes from the cell periphery to the TGN [57]. Recent proteomic analyses identified SNX6 as an autophagosome component, suggesting a role for the retromer complex in mTOR-dependent autophagy [58]. Decreased levels of the COPII vesicle coat SEC24D protein were detected in the *BCS1L* mutant fibroblasts. The COPII vesicle coat promotes the anterograde transport of newly synthesized membrane proteins from the endoplasmic reticulum (ER) to the TGN, where SEC24 protein isoforms (A, B, C and D) mediate the selective export of ER transmembrane proteins by involving lipid rafts as early sorting platforms [59].

These observations suggest a general up-regulation of the sorting machineries of transmembrane proteins to endosomes and lysosomes, probably as a way to retrieve important molecules for re-use in detriment of *de novo* protein synthesis, more energy consuming, or alternatively to get rid of dysfunctional organelles or molecules that might otherwise accumulate as a consequence of permanent oxidative damage. In agreement, our group has recently demonstrated that *BCS1L* mutant fibroblasts show increased bulk autophagy and an accumulation of vesicles, autophagic vacuoles and lysosomes as a result of a partial blockage of the autophagic flux [60]. This could be a consequence of the predicted cytoskeleton destructuration, since endosomal protein sorting requires localized polymerization of actin filaments and microtubules [57, 61].

Alterations in cellular stress responses

Metabolic and oxidative stress could elicit the activation of cellular stress responses in the *BCS1L* mutant fibroblasts, as evidenced by the raised levels of ER chaperones that take part in the *Unfolded Protein Response* (UPR), such as GRP78,

1 ERP29 and ERP70. This mechanism is activated in response to the accumulation of
2 unfolded or misfolded proteins to restore the normal cellular functions by halting
3 protein translation and activating signaling pathways that increase the expression of
4 molecular chaperones that target oxidized proteins for proteasomal degradation [62].
5 Prolonged failure to adapt to ER stress will result in the UPR aiming towards apoptosis,
6 which could explain the increased cell death observed in *BCS1L* mutant fibroblasts [22].

7 PARK7/DJ-1 protein levels were also increased in the mutant cells. DJ-1 plays an
8 important protective role against oxidative stress and cell death. Under normal
9 conditions, DJ-1 is predominantly located in the cytoplasm and, in response to oxidative
10 stress, it translocates to the mitochondrion and subsequently to the nucleus, where it acts
11 as a redox sensitive chaperone. Within mitochondria, it seems to cooperate with the
12 PINK1/parkin machinery to regulate the correct function and morphology of the
13 mitochondrial network and for the autophagy of dysfunctional mitochondria [63, 64].
14 Possibly, the metabolic and oxidative stress observed in the *BCS1L* mutant fibroblasts
15 might induce the expression of proteins with protective roles against ROS and cell death
16 induction. These expression variations probably imply further alterations in gene
17 expression to promote cellular adaptations to metabolic and oxidative damage.

18 **CONCLUSIONS**

19 The DIGE technology has allowed us to obtain a protein profile characteristic for
20 fibroblasts with mutations in *BCS1L*. Current evidence suggests a general defect in
21 energy metabolism and a shift towards anaerobic glycolysis and catabolic processes as
22 alternative ways to obtain ATP, and a whole cellular genetic and metabolic
23 reprogramming to adapt cell survival to mitochondrial dysfunction-elicited oxidative
24 stress. Gaining deeper insight into these functional adaptations will pave the way
25 towards biomarkers detection and future therapeutic strategies for complex III
26 deficiency.

ACKNOWLEDGEMENTS

Authors acknowledge Dr. P. Gómez-González, Dr. M. Martínez-Gomariz, Dr. J.C. González-Armas and Dr. I. García-Consuegra for manuscript revision and excellent technical support, and Dr. M. Vázquez López, Dr. A. Verdú and Dr. M.T. García Silva for kindly providing the patients' fibroblasts. The DIGE experiment was carried out at the Proteomics Facility UCM-PCM/ProteoRed (Madrid, Spain). This work was funded by Instituto de Salud Carlos III (grant numbers PI11-00182 to C.U., PS09-01359 to M.A.M., CP11-00151 to M.M., and PI12-00933 to S.C.), by Comunidad Autónoma de Madrid (P2010/BMD-2361 to C.U. and P2010/BMD-2402 to M.A.M. and S.C.) and by NIH-NIGMS (1R01GM105781-01 to C.U.).

REFERENCES

- [1] Baum H, Rieske JS, Silman HI, Lipton SH. On the mechanism of electron transfer in complex III of the electron transfer chain. *Proc Natl Acad Sci USA* 1967;57:798-805.
- [2] Iwata S, Lee JW, Okada K, Lee JK, Iwata M, Rasmussen B, et al. Complete structure of the 11-subunit bovine mitochondrial cytochrome bc₁ complex. *Science* 1998;281:64-71.
- [3] Xia D, Yu CA, Kim H, Xia JZ, Kachurin AM, Zhang L, et al. Crystal structure of the cytochrome bc₁ complex from bovine heart mitochondria. *Science* 1997;277:60-6.
- [4] Benit P, Lebon S, Rustin P. Respiratory-chain diseases related to complex III deficiency. *Biochim Biophys Acta* 2009;1793:181-5.
- [5] Andreu AL, Hanna MG, Reichmann H, Bruno C, Penn AS, Tanji K, et al. Exercise intolerance due to mutations in the cytochrome b gene of mitochondrial DNA. *New Engl J Med* 1999;341:1037-44.
- [6] de Lonlay P, Valnot I, Barrientos A, Gorbatyuk M, Tzagoloff A, Taanman JW, et al. A mutant mitochondrial respiratory chain assembly protein causes complex III deficiency in patients with tubulopathy, encephalopathy and liver failure. *Nat Genet* 2001;29:57-60.
- [7] Haut S, Brivet M, Touati G, Rustin P, Lebon S, Garcia-Cazorla A, et al. A deletion in the human QP-C gene causes a complex III deficiency resulting in hypoglycaemia and lactic acidosis. *Hum Genet* 2003;113:118-22.
- [8] Barel O, Shorer Z, Flusser H, Ofir R, Narkis G, Finer G, et al. Mitochondrial complex III deficiency associated with a homozygous mutation in UQCRCQ. *Am J Hum Genet* 2008;82:1211-6.
- [9] Ghezzi D, Arzuffi P, Zordan M, Da Re C, Lamperti C, Benna C, et al. Mutations in TTC19 cause mitochondrial complex III deficiency and neurological impairment in humans and flies. *Nat Genet* 2011;43:259-63.

- 1 [10] Miyake N, Yano S, Sakai C, Hatakeyama H, Matsushima Y, Shiina M, et al.
2 Mitochondrial complex III deficiency caused by a homozygous UQCRC2 mutation
3 presenting with neonatal-onset recurrent metabolic decompensation. *Hum Mutat*
4 2013;34:446-52.
- 5 [11] Wagener N, Ackermann M, Funes S, Neupert W. A Pathway of Protein
6 Translocation in Mitochondria Mediated by the AAA-ATPase Bcs1. *Mol Cell*
7 2011;44:191-202.
- 8 [12] Ramos-Arroyo MA, Hualde J, Ayechu A, De Meirleir L, Seneca S, Nadal N, et al.
9 Clinical and biochemical spectrum of mitochondrial complex III deficiency caused by
10 mutations in the BCS1L gene. *Clin Genet* 2009;75:585-7.
- 11 [13] Hinson JT, Fantin VR, Schonberger J, Breivik N, Siem G, McDonough B, et al.
12 Missense mutations in the BCS1L gene as a cause of the Bjornstad syndrome. *New*
13 *Engl J Med* 2007;356:809-19.
- 14 [14] Visapaa I, Fellman V, Vesa J, Dasvarma A, Hutton JL, Kumar V, et al. GRACILE
15 syndrome, a lethal metabolic disorder with iron overload, is caused by a point mutation
16 in BCS1L. *Am J Hum Genet* 2002;71:863-76.
- 17 [15] Blazquez A, Gil-Borlado MC, Moran M, Verdu A, Cazorla-Calleja MR, Martin
18 MA, et al. Infantile mitochondrial encephalomyopathy with unusual phenotype caused
19 by a novel BCS1L mutation in an isolated complex III-deficient patient. *Neuromuscul*
20 *Disord* 2009;19:143-6.
- 21 [16] De Meirleir L, Seneca S, Damis E, Sepulchre B, Hoorens A, Gerlo E, et al. Clinical
22 and diagnostic characteristics of complex III deficiency due to mutations in the BCS1L
23 gene. *Am J Med Genet* 2003;121A:126-31.
- 24 [17] Fernandez-Vizarra E, Bugiani M, Goffrini P, Carrara F, Farina L, Procopio E, et al.
25 Impaired complex III assembly associated with BCS1L gene mutations in isolated
26 mitochondrial encephalopathy. *Hum Mol Genet* 2007;16:1241-52.

- [18] Gil-Borlado MC, Gonzalez-Hoyuela M, Blazquez A, Garcia-Silva MT, Gabaldon T, Manzanares J, et al. Pathogenic mutations in the 5' untranslated region of BCS1L mRNA in mitochondrial complex III deficiency. *Mitochondrion* 2009;9:299-305.
- [19] Tuppen HA, Fehmi J, Czermin B, Goffrini P, Meloni F, Ferrero I, et al. Long-term survival of neonatal mitochondrial complex III deficiency associated with a novel BCS1L gene mutation. *Mol Genet Metab* 2010;100:345-8.
- [20] Al-Owain M, Colak D, Albakheet A, Al-Younes B, Al-Humaidi Z, Al-Sayed M, et al. Clinical and biochemical features associated with BCS1L mutation. *J Inherit Metab Dis* 2013;36:813-20.
- [21] Lynn AM, King RI, Mackay RJ, Florkowski CM, Wilson CJ. BCS1L gene mutation presenting with GRACILE-like syndrome and complex III deficiency. *Ann Clin Biochem* 2012;49:201-3.
- [22] Moran M, Marin-Buera L, Gil-Borlado MC, Rivera H, Blazquez A, Seneca S, et al. Cellular pathophysiological consequences of BCS1L mutations in mitochondrial complex III enzyme deficiency. *Hum Mutat* 2010;31:930-41.
- [23] Leveen P, Kotarsky H, Morgelin M, Karikoski R, Elmer E, Fellman V. The GRACILE mutation introduced into Bcs1l causes postnatal complex III deficiency: A viable mouse model for mitochondrial hepatopathy. *Hepatology* 2011;53:437-447.
- [24] Tamai S, Iida H, Yokota S, Sayano T, Kiguchiya S, Ishihara N, et al. Characterization of the mitochondrial protein LETM1, which maintains the mitochondrial tubular shapes and interacts with the AAA-ATPase BCS1L. *J Cell Sci* 2008;121:2588-600.
- [25] Fellman V. The GRACILE syndrome, a neonatal lethal metabolic disorder with iron overload. *Blood Cells Mol Dis* 2002;29:444-50.
- [26] Kanehisa M, Goto S, Sato Y, Furumichi M, Tanabe M. KEGG for integration and interpretation of large-scale molecular data sets. *Nucleic Acids Res* 2012;40:D109-14.

- [27] Franceschini A, Szklarczyk D, Frankild S, Kuhn M, Simonovic M, Roth A, et al. STRING v9.1: protein-protein interaction networks, with increased coverage and integration. *Nucleic Acids Res* 2013;41:D808-15.
- [28] Knerr I, Weinhold N, Vockley J, Gibson KM. Advances and challenges in the treatment of branched-chain amino/keto acid metabolic defects. *J Inherit Metab Dis* 2012;35:29-40.
- [29] Tretter L, Adam-Vizi V. Generation of reactive oxygen species in the reaction catalyzed by alpha-ketoglutarate dehydrogenase. *J Neurosci* 2004;24:7771-8.
- [30] Starkov AA, Fiskum G, Chinopoulos C, Lorenzo BJ, Browne SE, Patel MS, et al. Mitochondrial alpha-ketoglutarate dehydrogenase complex generates reactive oxygen species. *J Neurosci* 2004;24:7779-88.
- [31] Kotarsky H, Keller M, Davoudi M, Leveen P, Karikoski R, Enot DP, et al. Metabolite profiles reveal energy failure and impaired beta-oxidation in liver of mice with complex III deficiency due to a BCS1L mutation. *PLoS One* 2012;7:e41156.
- [32] Lavery GG, Walker EA, Turan N, Rogoff D, Ryder JW, Shelton JM, et al. Deletion of hexose-6-phosphate dehydrogenase activates the unfolded protein response pathway and induces skeletal myopathy. *J Biol Chem* 2008;283:8453-61.
- [33] Hintze KJ, Theil EC. DNA and mRNA elements with complementary responses to hemin, antioxidant inducers, and iron control ferritin-L expression. *Proc Natl Acad Sci USA* 2005;102:15048-52.
- [34] Yang J, Valineva T, Hong J, Bu T, Yao Z, Jensen ON, et al. Transcriptional co-activator protein p100 interacts with snRNP proteins and facilitates the assembly of the spliceosome. *Nucleic Acids Res* 2007;35:4485-94.
- [35] Schreiber KH, Kennedy BK. When lamins go bad: nuclear structure and disease. *Cell* 2013;152:1365-75.

- 1 [36] Gu Y, Jin S, Gao Y, Weaver DT, Alt FW. Ku70-deficient embryonic stem cells
2 have increased ionizing radiosensitivity, defective DNA end-binding activity, and
3 inability to support V(D)J recombination. *Proc Natl Acad Sci USA* 1997;94:8076-81.
- 4 [37] Chapman JR, Taylor MR, Boulton SJ. Playing the end game: DNA double-strand
5 break repair pathway choice. *Mol Cell* 2012;47:497-510.
- 6 [38] Li L, Monckton EA, Godbout R. A role for DEAD box 1 at DNA double-strand
7 breaks. *Mol Cell Biol* 2008;28:6413-25.
- 8 [39] Padmanabhan B, Kuzuhara T, Adachi N, Horikoshi M. The crystal structure of
9 CCG1/TAF(II)250-interacting factor B (CIB). *J Biol Chem* 2004;279:9615-24.
- 10 [40] Svitkin YV, Yanagiya A, Karetnikov AE, Alain T, Fabian MR, Khoutorsky A, et
11 al. Control of translation and miRNA-dependent repression by a novel poly(A) binding
12 protein, hnRNP-Q. *PLoS Biol* 2013;11:e1001564.
- 13 [41] Kim DY, Kim W, Lee KH, Kim SH, Lee HR, Kim HJ, et al. hnRNP Q regulates
14 translation of p53 in normal and stress conditions. *Cell Death Differ* 2013;20:226-34.
- 15 [42] Wong TS, Rajagopalan S, Townsley FM, Freund SM, Petrovich M, Loakes D, et
16 al. Physical and functional interactions between human mitochondrial single-stranded
17 DNA-binding protein and tumour suppressor p53. *Nucleic Acids Res* 2009;37:568-81.
- 18 [43] Mikhailov VS, Bogenhagen DF. Termination within oligo(dT) tracts in template
19 DNA by DNA polymerase gamma occurs with formation of a DNA triplex structure
20 and is relieved by mitochondrial single-stranded DNA-binding protein. *J Biol Chem*
21 1996;271:30774-80.
- 22 [44] Barrett T, Xiao B, Dodson EJ, Dodson G, Ludbrook SB, Nurmahomed K, et al.
23 The structure of the GTPase-activating domain from p50rhoGAP. *Nature*
24 1997;385:458-61.

- [45] Fukata Y, Itoh TJ, Kimura T, Menager C, Nishimura T, Shiromizu T, et al. CRMP-2 binds to tubulin heterodimers to promote microtubule assembly. *Nat Cell Biol* 2002;4:583-91.
- [46] Saarikangas J, Barral Y. The emerging functions of septins in metazoans. *EMBO Rep* 2011;12:1118-26.
- [47] Yin HL, Stossel TP. Control of cytoplasmic actin gel-sol transformation by gelsolin, a calcium-dependent regulatory protein. *Nature* 1979;281:583-6.
- [48] Rostovtseva TK, Sheldon KL, Hassanzadeh E, Monge C, Saks V, Bezrukov SM, et al. Tubulin binding blocks mitochondrial voltage-dependent anion channel and regulates respiration. *Proc Natl Acad Sci USA* 2008;105:18746-51.
- [49] Cassimeris L, Silva VC, Miller E, Ton Q, Molnar C, Fong J. Fueled by microtubules: does tubulin dimer/polymer partitioning regulate intracellular metabolism? *Cytoskeleton* 2012;69:133-43.
- [50] Al-Mulla F, Bitar MS, Taqi Z, Yeung KC. RKIP: much more than Raf kinase inhibitory protein. *J Cell Physiol* 2013;228:1688-702.
- [51] Monastyrskaya K, Babiychuk EB, Draeger A. The annexins: spatial and temporal coordination of signaling events during cellular stress. *Cell Mol Life Sci* 2009;66:2623-42.
- [52] Rescher U, Ruhe D, Ludwig C, Zobiack N, Gerke V. Annexin 2 is a phosphatidylinositol (4,5)-bisphosphate binding protein recruited to actin assembly sites at cellular membranes. *J Cell Sci* 2004;117:3473-80.
- [53] Vedeler A, Hollas H, Grindheim AK, Raddum AM. Multiple roles of annexin A2 in post-transcriptional regulation of gene expression. *Curr Prot Pept Sci* 2012;13:401-12.
- [54] Mayran N, Parton RG, Gruenberg J. Annexin II regulates multivesicular endosome biogenesis in the degradation pathway of animal cells. *EMBO J* 2003;22:3242-53.

- [55] Jeon YJ, Kim DH, Jung H, Chung SJ, Chi SW, Cho S, et al. Annexin A4 interacts with the NF-kappaB p50 subunit and modulates NF-kappaB transcriptional activity in a Ca²⁺-dependent manner. *Cell Mol Life Sci* 2010;67:2271-81.
- [56] McGough II, Cullen PJ. Recent advances in retromer biology. *Traffic* 2011;12:963-71.
- [57] Hong Z, Yang Y, Zhang C, Niu Y, Li K, Zhao X, et al. The retromer component SNX6 interacts with dynactin p150(Glued) and mediates endosome-to-TGN transport. *Cell Res* 2009;19:1334-49.
- [58] Dengjel J, Hoyer-Hansen M, Nielsen MO, Eisenberg T, Harder LM, Schandorff S, et al. Identification of autophagosome-associated proteins and regulators by quantitative proteomic analysis and genetic screens. *Mol Cell Proteomics* 2012;11:M111 014035.
- [59] Bonnon C, Wendeler MW, Paccaud JP, Hauri HP. Selective export of human GPI-anchored proteins from the endoplasmic reticulum. *J Cell Sci* 2010;123:1705-15.
- [60] Moran M, Delmiro A, Blazquez A, Ugalde C, Arenas J, Martin MA. Bulk autophagy, but not mitophagy, is increased in cellular model of mitochondrial disease. *Biochim Biophys Acta* 2014;1842:1059-70.
- [61] Seaman MN, Gautreau A, Billadeau DD. Retromer-mediated endosomal protein sorting: all WASHed up! *Trends Cell Biol* 2013;23:522-8.
- [62] Hetz C. The unfolded protein response: controlling cell fate decisions under ER stress and beyond. *Nat Rev Mol Cell Biol* 2012;13:89-102.
- [63] Hao LY, Giasson BI, Bonini NM. DJ-1 is critical for mitochondrial function and rescues PINK1 loss of function. *Proc Natl Acad Sci USA* 2010;107:9747-52.
- [64] Thomas KJ, McCoy MK, Blackinton J, Beilina A, van der Brug M, Sandebring A, et al. DJ-1 acts in parallel to the PINK1/parkin pathway to control mitochondrial function and autophagy. *Hum Mol Genet* 2011;20:40-50.

FIGURE LEGENDS

Figure 1. Oxygen consumption, ATP levels and glycolytic flux in complex III-

deficient fibroblasts. (A) Real-time analysis of oxygen consumption rates (OCR) in

control (n=4) and patients' fibroblasts (n=3) respiring in 1 g/l glucose-containing

medium. Student's *t* test: ***($p < 0.001$). (B) Intracellular ATP content in control (n=4)

and patient's fibroblasts (n=4) grown in 1 g/l glucose-containing medium. Mann-

Whitney *U* test: **($p < 0.01$) (C) Extracellular acidification rates (ECAR) as an indicator

of lactate release to the extracellular medium in control (n=4) and patient's fibroblasts

(n=3). All measurements were performed at least six times per sample. Data are

expressed as percentages of the mean values obtained in controls \pm standard deviation.

Figure 2. DIGE experimental design. Fibroblasts were obtained from age and sex-

matched control individuals (C1-C4) and complex III-deficient patients (P1-P4). Cells

were balanced for passage number and homogenized prior to protein extraction. Whole

cell extracts were purified and labeled with the corresponding Cy dyes. Samples were

then mixed and resolved on four independent DIGE gels. Three fluorescence images

were obtained from each gel and subjected to image analysis using DeCyder software.

After biological variation analysis, spots that exhibited significant quantity

modifications in patients' fibroblasts were identified by MALDI-TOF/ TOF mass

spectrometry. Finally, extended data analysis (EDA) and KEGG and STRING database

searches were carried out to gain further information about protein alterations that are

inherent to complex III deficiency.

Figure 3. Representative Cy2-labeled internal standard proteome map indicating

the proteins altered in complex III-deficient fibroblasts. Proteins were resolved in a

3–11 (nonlinear) pH range on the first dimension and on 12% acrylamide gels on the

second dimension. Proteins that exhibited significant expression alterations in patients'

samples were identified by MALDI-TOF or MALDI-TOF/TOF mass spectrometry. These proteins are listed in Table 1 by the same number as that in the figure.

Figure 4. Unsupervised multivariate analysis of the DIGE assay. (A) Principal component analysis clustered the 8 individual Cy3- and Cy5-labeled expression maps into control (*orange*) or patients' (*green*) groups differentiated by two principal components that distinguish the variance. (B) *k*-means cluster analysis showing the four different clusters that group the identified proteins. *q*, cluster quality; *no*, number of proteins belonging to each cluster. The set of proteins corresponding to each cluster is listed in Supplemental Table S2. (C) Unsupervised hierarchical clustering of the 8 independent images based on the global expression patterns of the 52 protein spots that were altered in complex III-deficient fibroblasts. Clustering of individual samples is shown on *top* with the DIGE gel number and type of dye labeling for each sample listed at the *bottom*. Clustering of individual proteins is shown on the *left* with relative expression values displayed as an expression matrix (heat map) using a standardized log abundance scale ranging from negative values (*green*) to positive values (*red*), and the spot numbers are listed along the *right side*. These numbers are in agreement with those listed in Table 1. ↑P and ↓P, proteins whose expression is up- and down-regulated, respectively.

Figure 5. DIGE assay validation. (A) Western-blot analysis of differentially-expressed proteins in *BCS1L* mutant fibroblasts. 10 µg of whole cell protein lysates were separated on 10% SDS-PAGE gels, blotted into nitrocellulose membranes and incubated with the indicated antibodies. (B) Quantitative changes in band intensities were evaluated by densitometric scanning with the Image J software. Signals from at least three independent experiments per sample were quantified; the densitometric mean values of the patients' fibroblasts (n=4) were normalized to those of the loading control β-actin, and expressed as percentages of the mean control values (n=4, horizontal bar) ±

standard deviation. (a.d.u.), arbitrary densitometric units. (C) For the detection of the indicated proteins, indirect immunofluorescence was performed at least in duplicate per sample in fixed controls (n=3) and patients' fibroblasts (n=4). A representative image is shown.

Figure 6. Physiological validation of putative functional adaptations of human fibroblasts to mitochondrial respiratory chain complex III enzyme deficiency.

Glycolysis up-regulation was assessed by enzymatic measurements of (A) cytosolic GAPDH and (B) mitochondrial PDH activities in the *BCS1L* mutant fibroblasts (n=4) and controls (n=4). Data are expressed as the mean values of three independent measurements per sample \pm standard deviation. (a.d.u.), arbitrary densitometric units.

(C) Amino acids concentrations of serum-free cell culture media from control and *BCS1L* mutant fibroblasts. To determine the amino acids concentrations, cationic exchange chromatography was performed in triplicate per sample. Data are expressed as the mean values obtained from controls (n=4) and from the four patients' fibroblasts \pm standard deviation.

Figure 7. Hypothetical model of the functional adaptations of human fibroblasts to mitochondrial respiratory chain complex III enzyme deficiency.

Mutations in the *BCS1L* assembly factor cause severe complex III enzyme deficiency, which hampers oxygen consumption and ATP synthesis. A metabolic switch towards glycolysis and protein catabolism probably occurs in an attempt to maintain the intracellular ATP levels, increasing the ATP productive phase of glycolysis (1, 2 and 3) and decreasing the pyruvate dehydrogenase and Krebs cycle activities (4, 5). These events would lead to the accumulation of intermediate metabolites and amino acids (5, 6). A blockage of the pentose phosphate pathway (7, 8) could also be inferred, which would affect the synthesis of purines and pyrimidines and therefore nucleic / ribonucleic acids formation, resulting in an increased AMP/ATP ratio (9, 10). The detoxifying glutathione

metabolism would also be affected, which would amplify ROS damage (11). Eventually, the degradation of extracellular matrix components could take place as an alternative way to obtain energy (12), as well as alterations in the iron homeostasis (13) and the breakdown of the cytoskeleton architecture (14). These events could lead to alterations in the regulation of gene expression (15, 16 and 17), in intracellular trafficking and signal transduction mechanisms (18), as well as provoke a raise in the cellular responses to the oxidative and metabolic stress (19). Proteins whose levels were increased in the *BCS1L* mutant fibroblasts compared to the controls are indicated in red, and those whose levels were decreased are shown in green. Abbreviations are in accordance with the gene identity of proteins listed in Table 1.

Table 1. Proteins identified by 2-D DIGE-MS as differentially expressed in complex III-deficient fibroblasts grouped according to their predicted biological function.

Spot No.	Gene ID ^a	Swiss-Prot ^a	Protein name	Av.ratio ^b	t test	Cellular role	Loc. ^c	Score ^d	No.pept. / Number of mass values ^e	Cov. (%) ^f
Metabolism										
3	MTHFD1	P11586	C-1-tetrahydrofolate synthase	-1.53	0.013	One-carbon metabolism; Tetrahydrofolate interconversion	Cyt	176	25/65	31
9 mix	H6PD	O95479	Hexose-6-phosphate dehydrogenase	-1.24	0.037	Pentose phosphate pathway	Cyt / ER	62	12/65	17
17	ENO1	P06733	Alpha-enolase	1.3	0.03	Glycolysis	Cyt	104	15/65	37
23 mix	DLD	P09622	Dihydrolipoyl dehydrogenase	-1.35	0.036	Pyruvate decarboxylation; TCA cycle; Mitochondrial glycine cleavage system	Mit	70	NLGLEELGIELDPR.G (46)	7
23 mix	G6PD	P11413	Glucose-6-phosphate 1-dehydrogenase	-1.35	0.036	Pentose phosphate pathway	Cyt	58	NSYVAGQYDDAASYQ R.L (43)	6
25	DLST	P36957	Dihydrolipoyl lysine-residue succinyltransferase	-1.63	0.019	TCA cycle	Mit	154	16/34	31
30	ALDOA	P04075	Fructose-bisphosphate aldolase A	-1.79	0.04	Glycolysis	Cyt	144	17/65	59
32 mix	GAPDH	P04406	Glyceraldehyde-3-phosphate dehydrogenase	1.86	0.031	Glycolysis	Cyt	122	17/59	50
36	GNPDA1	P46926	Glucosamine-6-phosphate isomerase 1	1.51	0.012	Aminosugars metabolism	Cyt	82	12/51	38
39 mix	PGLS	O95336	6-phospho gluconolactonase	1.55	0.0064	Pentose phosphate pathway	Cyt	133	WTLGFCDER.L (9) LLTVPFKEKHSTL.- (29) IVAPISDSPKPPPPQR.V (37)	36
43	APRT	P07741	Adenine phosphoribosyl transferase	1.33	0.037	AMP formation via purine ribonucleoside salvage	Cyt	99	9/39	57
45	FTL	P02792	Ferritin light chain	2.2	0.021	Iron homeostasis	Cyt	82	9/31	46
Regulation of Gene Expression										
2 mix	SND1	Q7KZF4	Staphylococcal nuclease domain-containing protein 1	-1.32	0.036	Transcriptional coactivator	Nuc	187	26/65	32
9 mix	DDX1	Q92499	ATP-dependent RNA helicase DDX1	-1.24	0.037	Transcriptional coactivator;	Nuc	207	28/65	45

						mRNA processing				
13	XRCC6	P12956	X-ray repair cross-complementing protein 6	-1.48	0.018	Involved in DNA non-homologous end joining, required for double-strand break repair and DNA somatic recombination	Nuc	72	13/65	24
14	XRCC6	P12956	X-ray repair cross-complementing protein 6	-2.11	0.0034	Involved in DNA non-homologous end joining, required for double-strand break repair and DNA somatic recombination	Nuc	106	13/32	23
18	SYNCRIP	O60506	Heterogeneous nuclear ribonucleoprotein Q (hnRNP Q)	1.26	0.024	mRNA processing and stability mechanisms	Nuc	168	23/56	33
19	LMNA	P02545	Lamin-A/C	-1.65	0.028	Nuclear lamina component; Involved in nuclear membrane architecture, chromatin organization, and telomere dynamics	Nuc	158	TALINSTGEEVAMR.K (13) VAVEEVDEEGKFVR.L (70) NSNLVGAAHEELQQSR .I (43)	15
21 mix	NARS	O43776	Asparagine-tRNA ligase	2.18	0.0067	tRNA aminoacylation for protein translation	Cyt	80	13/65	29
31	EIF3H	O15372	Eukaryotic translation initiation factor 3 subunit H	-1.22	0.017	Protein synthesis	Cyt	76	LFKPPQPPAR.M (6) GEPPLPEEDLSK.L (25) QSRGEPPLPEEDLSK.L (20)	12
42	ABHD14B	Q96IU4	Alpha/beta hydrolase domain-containing protein 14B	1.35	0.035	Putative transcriptional activator	Nuc	68	6/17	34
52 mix	SSBP1	Q04837	Mitochondrial single-stranded DNA-binding protein (mtSSB)	3.83	0.047	Mitochondrial DNA replication	Mit	93	12/65	61
Cytoskeleton formation and maintenance										
1	VCL	P18206	Vinculin	-1.42	0.041	Actin cytoskeleton; Cell-matrix and cell-cell adhesion	Cyt / PM	264	42/65	37
4	GSN	P06396	Gelsolin	2.97	0.017	Assembly / disassembly of actin filaments	Cyt	73	13/65	18
5	GSN	P06396	Gelsolin	1.95	0.023	Assembly / disassembly of actin filaments	Cyt	106	17/65	24
6	GSN	P06396	Gelsolin	1.92	0.032	Assembly / disassembly of actin	Cyt	77	12/48	16

						filaments				
8	GSN	P06396	Gelsolin	3.39	0.042	Assembly / disassembly of actin filaments	Cyt	61	12/60	17
10	MSN	P26038	Moesin	-1.47	0.032	Connections between plasma membranes and actin-based cytoskeletons	Cyt / PM	158	26/53	31
11	MSN	P26038	Moesin	-1.52	0.011	Connections between plasma membranes and actin-based cytoskeletons	Cyt / PM	116	25/65	30
20	WDR1	O75083	WD-repeat containing protein 1	-1.54	0.014	Disassembly of actin filaments	Cyt	103	9/15	16
21 mix	DPYSL2	Q16555	Dihydropyrimidinase- related protein 2 (CRMP-2)	2.18	0.0067	Cytoskeleton remodeling	Cyt	83	13/65	35
22	DPYSL2	Q16555	Dihydropyrimidinase- related protein 2 (CRMP-2)	2.92	0.037	Cytoskeleton remodeling	Cyt	189	25/65	52
24 mix	VIM	P08670	Vimentin	-1.33	0.03	Intermediate filaments component	Cyt	238	26/65	58
24 mix	TUBA1B	P68363	Tubulin alpha-1B chain	-1.33	0.03	Microtubules constituent	Cyt	197	22/65	50
26	ARHGAP1	Q07960	Rho GTPase-activating protein 1 (p50RhoGAP / CDC42GAP)	1.2	0.028	Rho protein mediated signal transduction; Actin cytoskeleton remodeling	Cyt / PM	108	15/65	33
27	SEPT11	Q9NVA2	Septin-11	1.39	0.029	Filament-forming cytoskeletal GTPase	Cyt	200	21/45	38
Intracellular trafficking and signal transduction										
2 mix	SEC24D	O94855	Protein transport protein SEC24D	-1.32	0.036	Anterograde protein transport from ER to Golgi	Cyt	67	18/65	17
28	SNX6	Q9UNH7	Sorting nexin-6	1.2	0.036	Retrograde protein transport from endosomes to the trans-Golgi network	Cyt	191	25/65	50
32 mix	ANXA2	P07355	Annexin A2	1.86	0.031	Endosomes sorting	Cyt / ECM	153	19/59	53
34	ANXA2	P07355	Annexin A2	2.06	0.044	Endosomes sorting	Cyt / ECM	211	20/35	45
37	ANXA4	P09525	Annexin A4	1.71	0.041	NF-kappaB signaling pathway; Possibly involved in exocytosis	Cyt	366	39/65	73
44	PEBP1	P30086	Phosphatidyl ethanolamine-binding protein 1	1.2	0.033	Serine protease inhibitor; Inhibits MAP kinase	Cyt	158	14/65	64

			(PEBP1 / RKIP)			cascade				
52 mix	PEBP1	P30086	Phosphatidyl ethanolamine-binding protein 1 (PEBP1 / RKIP)	3.83	0.047	Serine protease inhibitor; Inhibits MAP kinase cascade	Cyt	90	9/65	54
Cellular stress responses										
15 mix	PDIA4	P13667	Protein disulfide-isomerase A4 (ERP70)	1.67	0.05	Processing and folding of secretory proteins in the ER	ER	67	13/65	19
15 mix	HSPA5	P11021	78 kDa glucose-regulated protein (GRP78)	1.67	0.05	Unfolded protein response; Required for ER integrity and stress-induced autophagy	ER	309	35/65	47
16	HSPA5	P11021	78 kDa glucose-regulated protein (GRP78)	2.03	0.034	Unfolded protein response; Required for ER integrity and stress-induced autophagy	ER	418	41/65	55
39 mix	ERP29	P30040	Endoplasmic reticulum resident protein 29 (ERP29)	1.55	0.0064	Processing and folding of secretory proteins in the ER	ER	64	ILDQGEDFPASEMTR.I (31)	26
41	PARK7	Q99497	DJ-1	1.54	0.003	Redox sensor; Protects cells against oxidative stress; Transcriptional regulator; Maintenance of mitochondrial network morphology and mitophagy	Cyt / Mit / Nuc	86	10/21	43

Cyt, cytoplasmic; Nuc, nuclear; ER, endoplasmic reticulum; Mit, mitochondrial; ECM, extracellular matrix; PM, plasma membrane.

The first column (No.) indicates the protein spot numbers according to Fig. 3. Each spot was common to the total number (12) of gel images obtained in this analysis.

a Gene and protein identities and accession numbers according to GenBank and Uniprot/Swiss-Prot/TrEMBL databases, respectively.

b Average volume ratio OA/N quantified by DeCyder BVA module.

c Subcellular localization according to Uniprot database and PSORT information.

d Mascot MS protein score, or MS/MS ion score, obtained from MALDI-TOF/TOF spectra. In all cases, a probability score <0.01 was obtained.

e Number of peptide masses matching the top hit from MS-Fit PMF / Number of peptide masses searched. On each spot, the 65 most intense peaks were launched for search. When peptide sequence appears, the fragmentation ions score is indicated between brackets.

f Amino acid sequence coverage for the identified proteins.

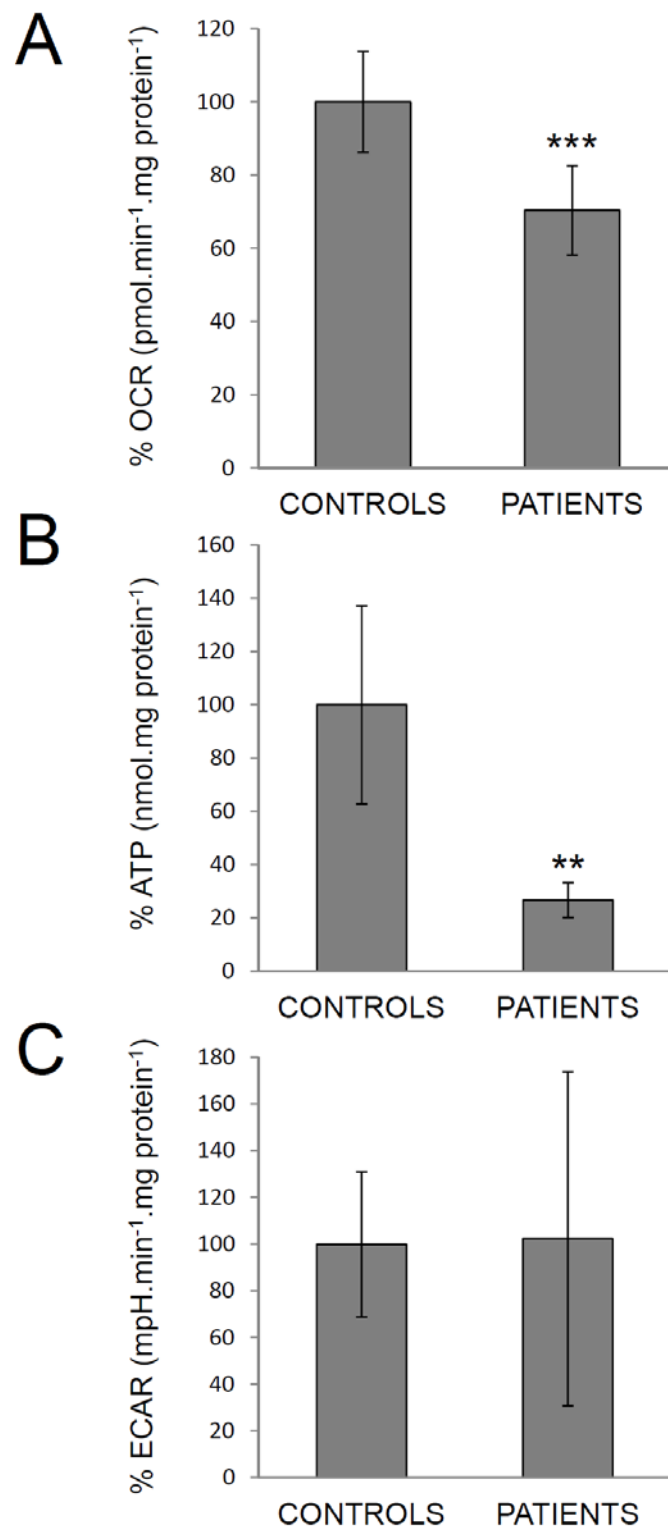


Figure 1

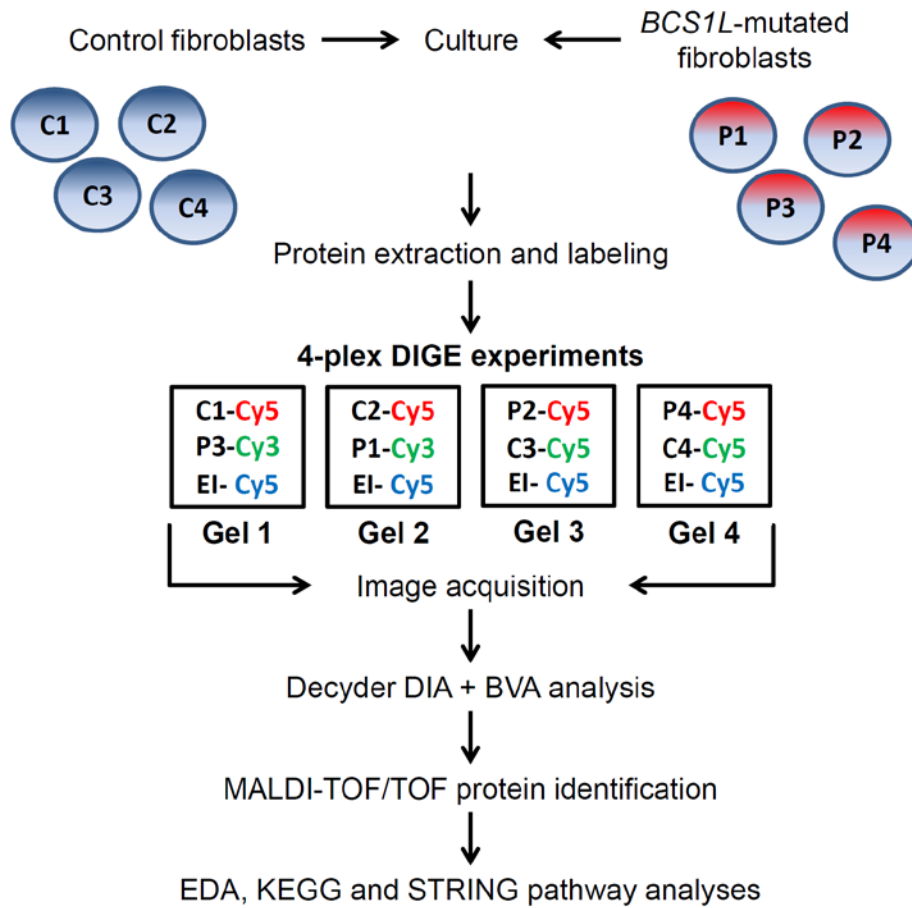


Figure 2

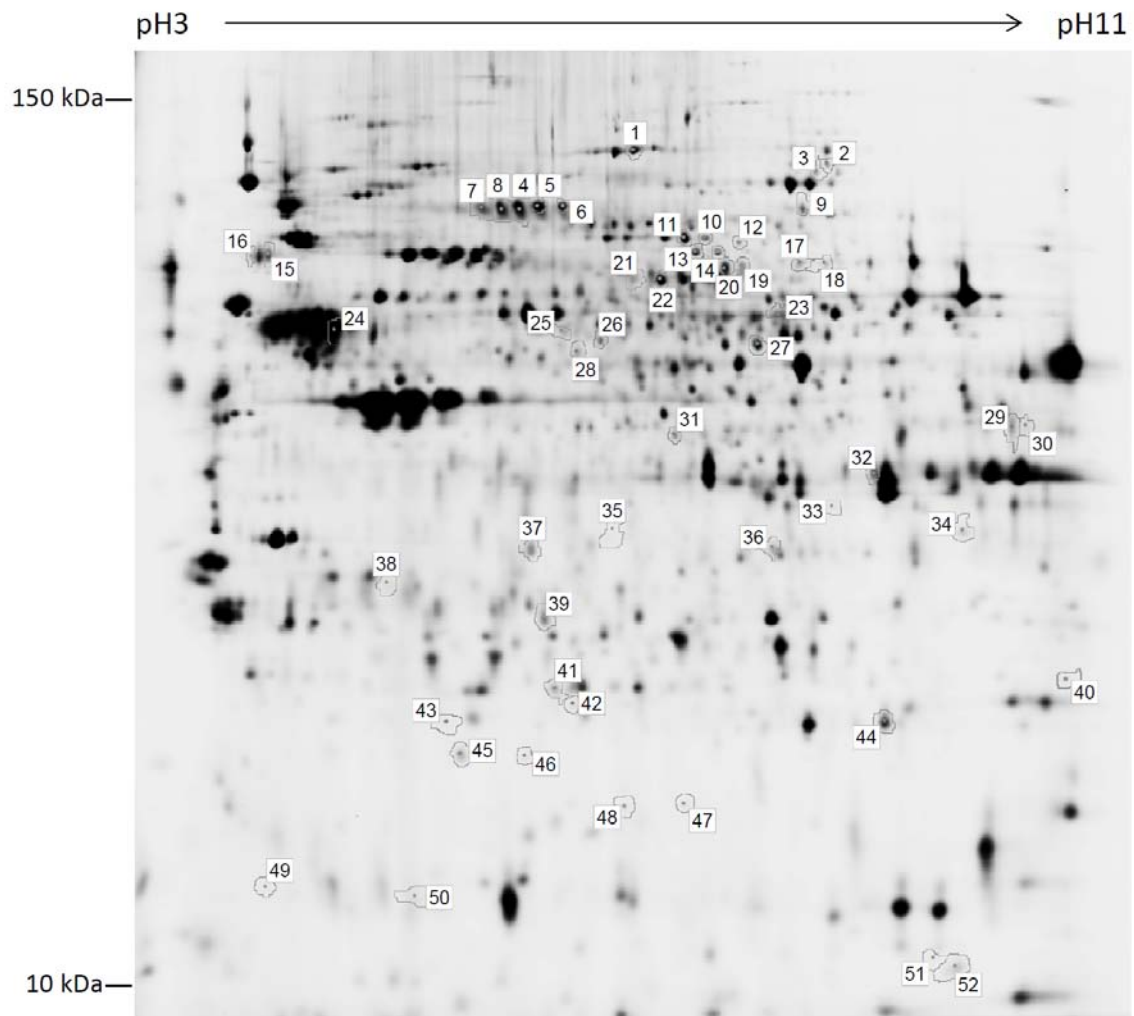


Figure 3

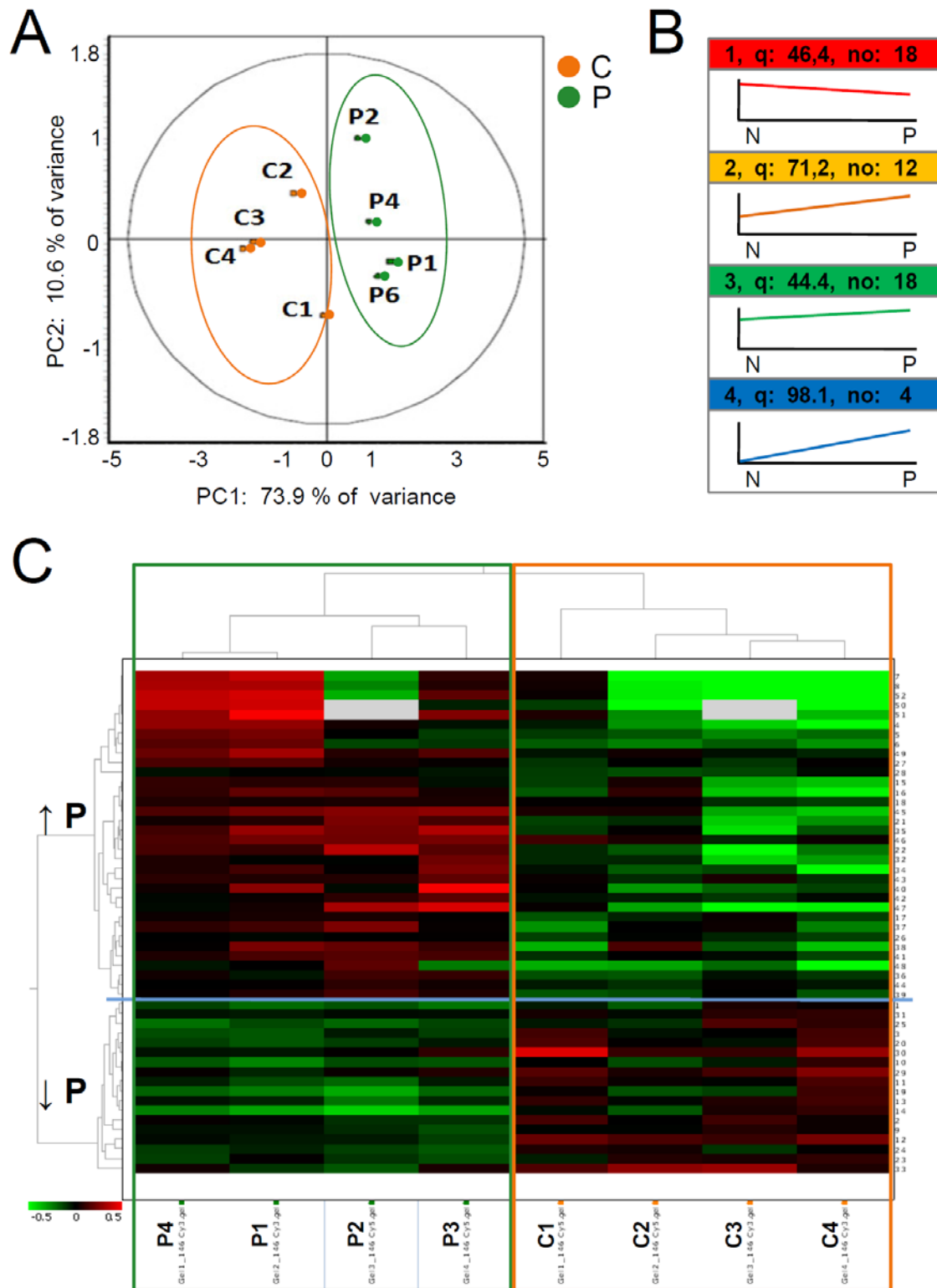


Figure 4

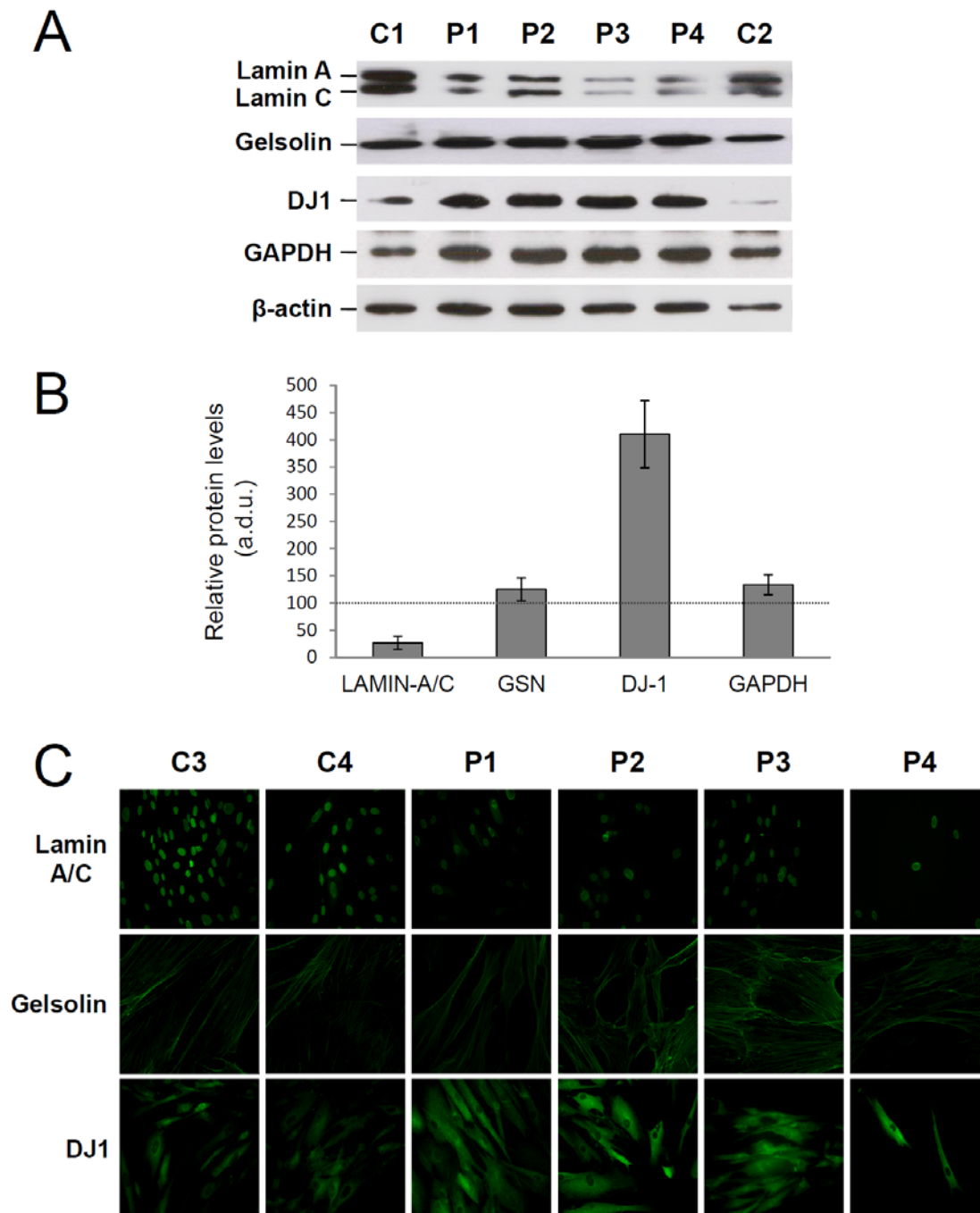


Figure 5

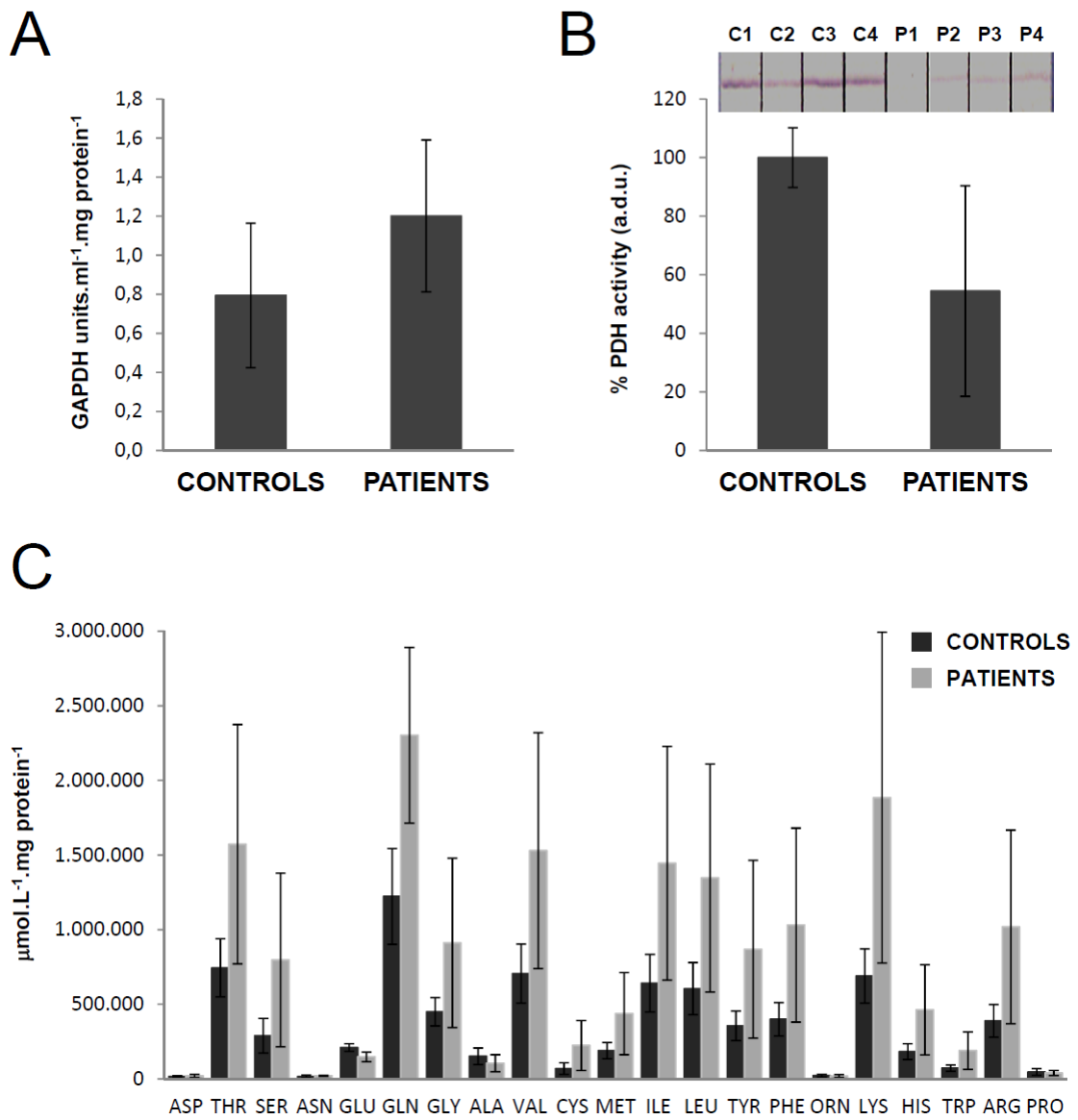


Figure 6

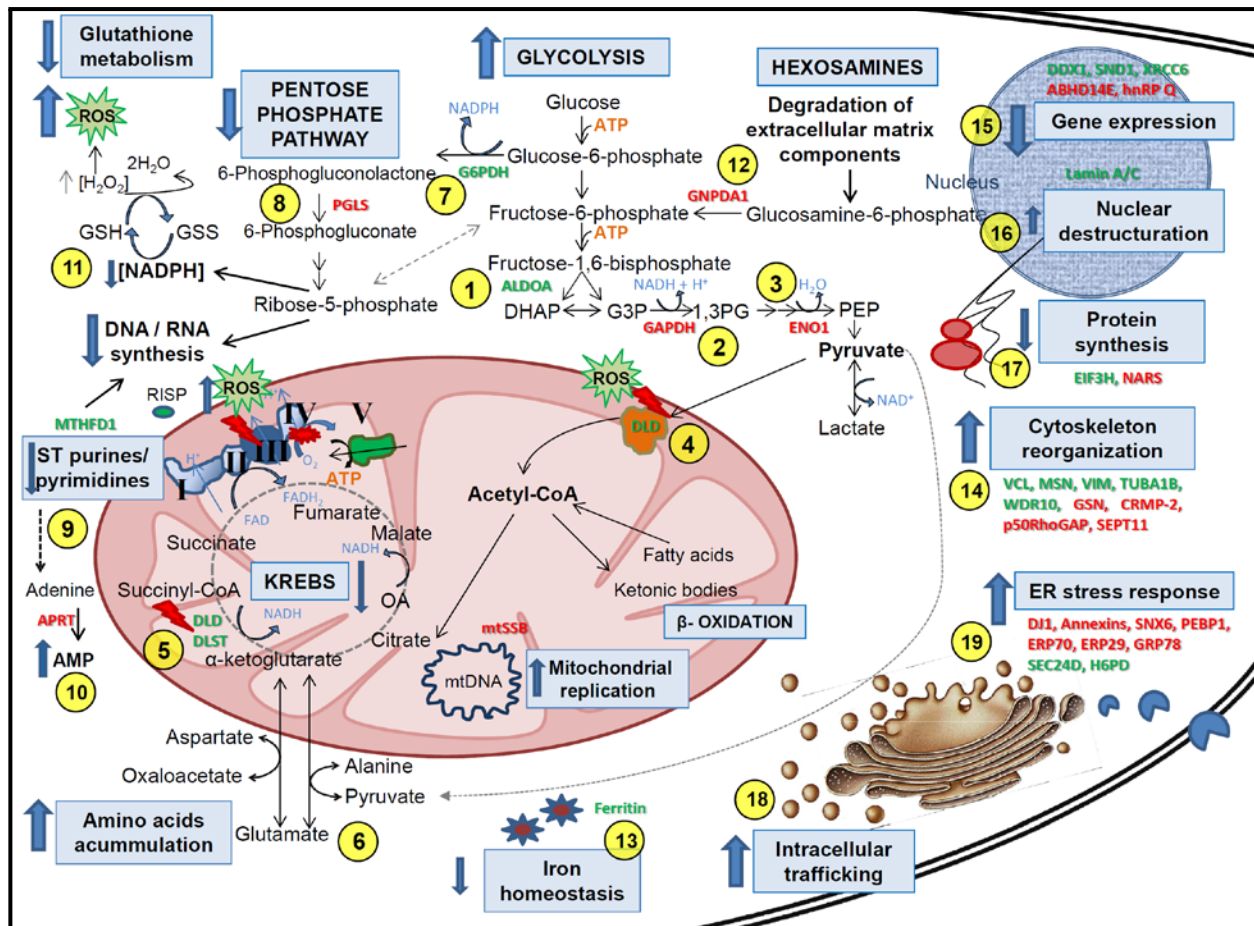


Figure 7